

3D modelling of clumpy PDRs

Understanding the Orion Bar stratification

S. Andree-Labsch¹, V. Ossenkopf¹, and M. Röllig¹

1. Physikalisches Institut, Universität zu Köln, Zùlpicher Straße 77, 50937 Köln
e-mail: sandree@ph1.uni-koeln.de

Received <date>; accepted <date>

ABSTRACT

Context. Models of photon-dominated regions (PDRs) still fail to fully reproduce some of the observed properties, in particular the combination of the intensities of different PDR cooling lines together with the chemical stratification, as observed e.g. for the Orion Bar PDR.

Aims. We aim to construct a self-consistent numerical PDR model to simulate full spectral cubes of line emission from arbitrary PDRs in three dimensions (3D). The model is to reproduce the intensity of the main cooling lines from the Orion Bar PDR and the observed layering structure of the different transitions.

Methods. Using a fractal description of the ISM combined with the KOSMA- τ PDR model, we build up a 3D compound, made of voxels (“3D pixels”), resembling the internal structure of a PDR. Each voxel contains “clumps” mimicking the fractal ISM. The local FUV field strength is calculated self-consistently for each voxel. Line emissivities and opacities of individual clumps, provided by the KOSMA- τ PDR model, are used to calculate voxel-averaged emissivities and opacities that are finally used to simulate full spectral cubes computing the radiative transport through the compound. To test the new model we try to simulate the structure of the Orion Bar PDR and compare the results to observations from HIFI/*Herschel* and from the Caltech Submillimetre Observatory (CSO).

Results. Our model is able to qualitatively reproduce the line intensities and the observed stratification of the emission structure in the various tracers based on the representation of the Orion Bar PDR by a clumpy edge-on cavity wall. In contrast, the model of a convex filament can be ruled out. In the cavity wall, a large fraction of the total mass needs to be contained in clumps. The mass of the interclump medium is constrained by the FUV penetration. Furthermore, the stratification profile cannot be reproduced by a model having the same amount of clump and interclump mass in each voxel, but dense clumps have to be removed from the PDR surface to reproduce the observed intensities and spatial structure.

Key words. photon-dominated region (PDR) – ISM: structure – ISM: clouds – submillimeter: ISM – infrared: ISM – radiative transfer

1. Introduction

Stars form from the ISM, in its dense and cold regions, inside molecular clouds. Hence, a better understanding of the chemical and physical processes inside molecular clouds, their internal structure, and the interaction between molecular clouds and the interstellar radiation field is an important step to constrain our knowledge on star formation processes.

Different components of the interstellar medium (ISM) are heated by the interstellar radiation field, originating from different sources and of different strength. A photon-dominated (or photo-dissociation) region (PDR) is a region in interstellar space where the photon energies fall below the ionisation energy of hydrogen, but where the interstellar far-UV (FUV) radiation field still dominates the heating processes and the chemistry of the ISM (photon energies: $6 \text{ eV} < h\nu < 13.6 \text{ eV}$). Here, the lower threshold of 6 eV is an estimate of the work function of a typical interstellar dust grain (see for example Hollenbach & Tielens 1999 and references therein) or (Fong et al. 2001). The main cooling processes are FIR continuum emission by dust grains, fine structure line emission by atoms and ions ([OI] $63 \mu\text{m}$ and $145 \mu\text{m}$, [CII] $158 \mu\text{m}$, [CI] $609 \mu\text{m}$ and $370 \mu\text{m}$, ...) and rotational and vibrational line emission by molecules (mainly CO) (Tielens & Hollenbach 1985; Hollenbach & Tielens 1999; Stern-

berg 2004). As PDR emission dominates the infrared and submillimetre spectra of star forming regions and galaxies (Röllig et al. 2007) they are the subject of many observations and extensive modelling. PDRs can be found in many different astrophysical scenarios, however, here we focus on the transition zone between HII- and molecular regions illuminated by the strong FUV radiation from young stars.

Many different PDR models have been developed aiming to relate the observed line and continuum emission to the physical parameters of the emitting region and to understand the physical processes taking place in PDRs. The models focus on different key aspects and exploit different geometries. An overview, emphasizing advantages and disadvantages of the different PDR models, can be found in the comparison study by Röllig et al. (2007).

In the molecular clouds the FUV field is attenuated, mainly due to absorption by dust grains. The decreasing FUV field strength causes a layered structure of different chemical transitions, referred to as *chemical stratification*, which can be observed in some PDRs, for example in the Orion Bar PDR (Tielens et al. 1993; van der Werf et al. 1996; Simon et al. 1997; van der Wiel et al. 2009).

In other PDRs, we find a spatial coexistence of different PDR tracers, that can be explained by a clumpy or filamentary

cloud structure (Stutzki et al. 1988; Stutzki & Guesten 1990; Howe et al. 1991). Actually, most observations of molecular clouds show filamentary, turbulent structures and substructures on all scales observed so far. Such clouds, like many other natural structures, can be described by fractal scaling laws. Fractal structures contain surfaces everywhere throughout the cloud, implying that a large fraction of the molecular material is located close to a surface and is hence exposed to the interstellar radiation field - i.e. forms PDRs (Ossenkopf et al. 2007). The fractal properties can be mimicked by an *ensemble* of clumps with an appropriate mass spectrum (Stutzki et al. 1998). Cubick et al. (2008) have shown that an ensemble of such clumps, immersed in a thin inter-clump medium, can be used to simulate the large scale fine structure emission from the Milky Way. Real PDRs will therefore always consist of a mixture of stratified surfaces with a fractal or clumpy molecular cloud structure.

This combination is not covered by the existing PDR models so far. For the Orion Bar PDR, one of the most prominent PDRs in the solar neighbourhood, a match between observations and simulation results of the high- J CO line intensities, combined with the observed stratification profile is still pending. Plane-parallel PDR models fail in this context, because a match of the high- J CO line intensities always requires a very sharp and dense PDR structure that is not consistent with the observed stratification covering, in the case of the Orion Bar PDR, at least 0.03 pc. More sophisticated models are necessary to reproduce the observed line intensities as well as the observed chemical stratification. To overcome this deficiency we have set up a PDR code which enables us to model clumpy star forming regions in 3D. The code supports a spatial variation of PDR parameters, like the mean density, the clump-size distribution, or the strength of the impinging FUV field.

At present most available PDR codes are designed to fit integrated line intensities. Hence, information contained in the line profiles is lost. To exploit this information the new code supports velocity dependent modelling which enables simulations of full line profiles.

In Sect. 2 we discuss the extension of the KOSMA- τ PDR model to a clumpy 3D PDR model. To test the new model we use selected observations of the Orion Bar PDR which are presented in Sect. 3. The 3D model of the Orion Bar PDR is presented in Sect. 4 and the fitting results are discussed in Sect. 5.1. The results are summarised in Sect. 6.

2. 3D PDR modelling

In this section we discuss the extension of the KOSMA- τ PDR model to a clumpy 3D PDR model. First the properties of the KOSMA- τ PDR model are summarised and modelling of the inhomogeneous ISM by fractal structures is discussed. Afterwards, the 3D model set-up is described including all steps which are necessary to simulate maps and spectra, comparable to astronomical observations.

2.1. KOSMA- τ PDR code

The KOSMA- τ model¹ (Röllig et al. 2006) has been developed at the University of Cologne in collaboration with the Tel-Aviv University. Contrary to many other models (compare Röllig et al. 2007 and references therein) which are based on plane-parallel geometries, the KOSMA- τ model utilises a spherical geometry, *clumps*, to model the structure of the PDR.

A single clump is parameterised by its total hydrogen mass M_{cl} , the surface hydrogen density $n_s = n_{\text{H},s} + 2n_{\text{H}_2,s}$ and the strength of the incident FUV field. The FUV flux is assumed to be isotropic and is measured in units of the Draine field integrated over the FUV range ($\chi_0 = 2.7 \cdot 10^{-3} \text{ erg s}^{-1} \text{ cm}^{-2}$, Draine 1978). In addition the model accounts for heating by cosmic rays at a constant rate of $2 \cdot 10^{-16} \text{ s}^{-1}$. In the model the radial density distribution $n(r)$ of the clumps is divided into a core and an outer region:

$$n(r) = n_s \cdot \begin{cases} \left(\frac{r}{R_{\text{cl}}}\right)^{-1.5}, & \text{for } 0.2 R_{\text{cl}} < r < R_{\text{cl}} \\ 11.18, & \text{for } r < 0.2 R_{\text{cl}} \end{cases} \quad (1)$$

where R_{cl} is the radius of the clump and $0.2 R_{\text{cl}}$ is the radius of the clump core. Consequently, the averaged density of one clump is given by

$$\bar{n}_{\text{cl}} = \frac{1}{\frac{4}{3}\pi R_{\text{cl}}^3} \cdot \int 4\pi r^2 n(r) dr \approx 1.91 n_s. \quad (2)$$

The clump averaged hydrogen column density, which is used to determine the clump averaged FUV absorption (see Sect. 2.3.2), is given by the same integral but averaged over the projected clump area πR_{cl}^2 which yields

$$\bar{N}_{\text{H,cl}} = 1.91 n_s \frac{4}{3} R_{\text{cl}}. \quad (3)$$

To analyze such a clump, the KOSMA- τ code iteratively solves the following steps: The chemical network, which can be assembled from a modular chemical network (Röllig et al. 2013), is used to derive local abundances, based on the local conditions. Using escape probabilities for the main cooling lines the local energy balance, i.e. heating and cooling processes are evaluated in steady state. After sufficient iterations, the line radiative transport through the clump is solved for lines of sight at different radial distances p from the centre point of the spherical clump.

Line intensities $I_{\text{cl}}(p)$ and opacities $\tau_{\text{cl}}(p)$ averaged over the projected clump surface

$$\bar{I}_{\text{cl}} = \frac{2}{R_{\text{cl}}^2} \int_0^{R_{\text{cl}}} I_{\text{cl}}(p) p dp \quad (4)$$

and

$$\bar{\tau}_{\text{cl}} = -\ln \left[\frac{2}{R_{\text{cl}}^2} \int_0^{R_{\text{cl}}} e^{-\tau_{\text{cl}}(p)} p dp \right] \quad (5)$$

have been derived for many molecular and atomic transitions, on a parameter grid of surface densities, clump masses and impinging FUV flux values.

2.2. Modelling the fractal ISM

The fractal structure of molecular clouds can be mimicked by a superposition of spherical clumps following a well-defined *clump-mass spectrum*, building up a *clumpy ensemble* (Stutzki et al. 1998; Cubick et al. 2008). The clump-mass spectrum can be described by a power-law

$$\frac{dN_{\text{cl}}}{dM_{\text{cl}}} = AM_{\text{cl}}^{-\alpha} \quad (6)$$

giving the number of clumps dN_{cl} in the mass bin dM_{cl} . In addition the masses of the clumps are related to their radii R_{cl} by the *mass-size relation*

$$M_{\text{cl}} = CR_{\text{cl}}^\gamma. \quad (7)$$

Typical values for the exponents are found to be $\alpha = 1.84$ and $\gamma = 2.31$ (Heithausen et al. 1998) meaning that smaller clumps are more numerous and denser.

¹ <http://www.astro.uni-koeln.de/kosma-tau>

2.2.1. Continuous description

Assuming that the masses of the clumps in an ensemble lie between a lower and an upper cutoff mass, m_l and m_u , one can derive the number of clumps N_{ens} in the ensemble (see Cubick et al. 2008):

$$N_{\text{ens}} = \frac{A}{\alpha - 1} (m_l^{1-\alpha} - m_u^{1-\alpha}) \quad \text{for } \alpha \neq 1 \quad (8)$$

and the total ensemble mass

$$M_{\text{ens}} = \frac{A}{2-\alpha} (m_u^{2-\alpha} - m_l^{2-\alpha}) \quad \text{for } \alpha \neq 2 \quad (9)$$

relating the constant A to the ensemble mass. For the observed values of α below two the total number of clumps in one ensemble is dominated by the low mass clumps, while most of the ensemble mass is provided by the high mass clumps. The constant C in Eq. 7 depends on the averaged ensemble density ρ_{ens} and the cutoff masses:

$$C = \left(\frac{4\pi}{3} \frac{2-\alpha}{1+3/\gamma-\alpha} \frac{m_u^{1+3/\gamma-\alpha} - m_l^{1+3/\gamma-\alpha}}{m_u^{2-\alpha} - m_l^{2-\alpha}} \rho_{\text{ens}} \right)^{\gamma/3}. \quad (10)$$

2.2.2. Discrete description

We use a discrete description for a simplified numerical treatment of the *clumpy ensemble* (compare Cubick 2005). Here, the mass spectrum of the clumps is not continuous, but represented by clumps with discrete masses $\{M_j\}_{j=1\dots n_M}$. We use a logarithmic parameter scale, i.e. $\frac{M_{j+1}}{M_j} = B$ with $B = 10$. Indices are ordered with increasing masses. For the Orion Bar simulations we used $M_{n_M} = 1 M_{\odot}$ whereas the simulations of the whole Milky Way by Cubick (2005) rather correspond to $M_{n_M} = 100 M_{\odot}$. We assume that the number of clumps N_j with mass M_j is given by the power law

$$N_j = A_d \cdot M_j^{1-\alpha} \quad (11)$$

with a constant A_d (d=discrete) similar to Eq. 8. This yields for the total mass M_J of clumps with mass M_j

$$M_J = M_j N_j = A_d \cdot M_j^{2-\alpha}. \quad (12)$$

For each ensemble the total mass of the ensemble M_{ens} and the averaged ensemble density ρ_{ens} are input parameters which can be fixed if the physical parameters of the PDR are known or they can be used as fitting parameters otherwise. The total ensemble mass is given by $M_{\text{ens}} = \sum_j N_j M_j$. Inserting N_j from Eq. 11 we find

$$A_d = \frac{M_{\text{ens}}}{\sum_j M_j^{2-\alpha}}. \quad (13)$$

The density of the individual clumps in the ensemble deviates from the ensemble averaged density ρ_{ens} according to the mass-size relation (Eq. 7), depending on their specific masses. For given masses $\{M_j\}_{j=1\dots n_M}$ the volumes $\{V_j\}_{j=1\dots n_M}$ of individual clumps can be calculated using Eq. 7 which yields

$$V_j = \frac{4}{3} \pi R_j^3 = \frac{4}{3} \pi \left(\frac{M_j}{C} \right)^{3/\gamma} \quad (14)$$

and consequently the averaged density of a clump is found to be

$$\rho_j = \frac{M_j}{V_j} = \frac{3}{4\pi} C^{3/\gamma} M_j^{1-3/\gamma}. \quad (15)$$

The ensemble averaged density ρ_{ens} is equal to the total ensemble mass, divided by the total ensemble volume

$$\rho_{\text{ens}} = \frac{\sum_j N_j M_j}{\sum_j N_j V_j} \quad (16)$$

and inserting Eq. 11 and Eq. 14 we derive

$$\rho_{\text{ens}} = \frac{3}{4\pi} C^{3/\gamma} \frac{\sum_j M_j^{2-\alpha}}{\sum_j M_j^{1+3/\gamma-\alpha}}. \quad (17)$$

Inserting Eq. 15 yields an expression for the density of clumps with mass M_j as a function of the average ensemble density.

$$\rho_j = \frac{M_j^{1-3/\gamma} \sum_k M_k^{1+3/\gamma-\alpha}}{\sum_k M_k^{2-\alpha}} \rho_{\text{ens}}. \quad (18)$$

In addition, the number of clumps N_j with mass M_j , as a function of the total ensemble mass, is found by combining Eqs. 11 and 13:

$$N_j = \frac{M_j^{1-\alpha}}{\sum_k M_k^{2-\alpha}} M_{\text{ens}}. \quad (19)$$

N_j as given by Eq. 19 and ρ_j given via Eq. 18 uniquely define the parameters of the overall ensemble.

In the 3D model the clumps of an ensemble are randomly distributed in a voxel with a known volume Δs^3 (compare Sect. 2.3.3). The volume filling factor, i.e. the fraction of the volume filled by clumps is given by

$$f_v = \frac{\sum_j N_j V_j}{\Delta s^3}. \quad (20)$$

In principle for the discrete description artificial cutoff masses can be chosen in such a way that the parameters of the discrete description match those of the continuous description. As the continuous description is not needed for the 3D PDR model, we will ignore this here and stick to the discrete description as an independent model.

2.3. Three-dimensional set-up

In irradiated molecular clouds we find position dependent conditions: the FUV field strength will decrease with increasing depth into the clouds due to absorption; furthermore, the average density and composition of the cloud may change. To model PDRs we set up a 3D model which can resemble arbitrary geometries using voxels. Each voxel contains at least one clumpy ensemble. Furthermore, a varying velocity information can be applied to each voxel, i.e. a velocity dispersion between the individual clumps, or a. The radiative transport (Sect. 2.3.4) enables the simulation of line integrated maps as well as the modelling of full line profiles.

2.3.1. Ensemble statistics: Area filling and clumps intersecting one line of sight

In the 3D set-up each ensemble is contained in a 3D voxel having a projected surface area Δs^2 perpendicular to the line of sight between the observer and the voxel². The clumps, building up

² The shape of the projected surface is arbitrary, but the volume should be spanned by the product of this surface area with the voxel depth. For the presented algorithm for example a cuboid or a cylinder could be used and give the same results. A different viewing angle to the same geometry, therefore needs a resampling of the density structure into new voxels where the z axis is parallel to the line of sight.

the ensemble, are randomly positioned in the voxel resulting in an area filling factor $N_j/\Delta s^2$ for each mass point j .

Consider one arbitrary line of sight, perpendicular to the projected area Δs^2 , through the ensemble. The probability distribution describing with how many randomly positioned clumps of mass M_j the line of sight intersects can be described by the binomial distribution

$$B(k_j | p_j, N_j) = \binom{N_j}{k_j} p_j^{k_j} (1 - p_j)^{N_j - k_j} \quad (21)$$

where k_j is the number of clumps pierced by the line of sight, p_j is the probability that the line of sight intersects with a specific clump of mass M_j and N_j is the total number of clumps with mass M_j . The intersection probability p_j is given by $p_j = \pi R_{cl,j}^2 / \Delta s^2$.

In the following Sects. 2.3.2 and 2.3.3 the binomial distribution (Eq. 21) is used to calculate ensemble averaged entities, namely the ensemble-averaged FUV extinction as well as ensemble-averaged line emissivities and opacities. To use binomial distributions as discrete probability distributions, the numbers of clumps, N_j , need to be integer values. This is not automatically provided by Eq. 19, however, scaling of the surface size Δs^2 (projected surface of the voxel = pixel) does not change the results for the ensemble-averaged entities, as long as the area filling factor $N_j/\Delta s^2$ is kept constant for each clump mass. Therefore, we rather consider a scaled "superpixel" of area $(\Delta s')^2 = \Delta s^2 \cdot c$ with a constant $c > 0$. Consequently, the numbers of clumps, N_j , need to be scaled accordingly: $N'_j = N_j \cdot c$. The constant c is chosen in a way that the following conditions are met:

- a) The projected clump area of the largest clumps needs to be smaller than the pixel area: $\pi R_{cl,n_M}^2 < \Delta s^2$, i.e. $p_{n_M} < 1$.
- b) The number of clumps with mass M_{n_M} is always an integer value.
- c) M_{n_M} is chosen to be the smallest value possible that does not contradict a) or b) to optimise for computing speed. This typically implies one clump with mass M_{n_M} .

After clump numbers and pixel surface area have been scaled the numbers of clumps $N_{j \neq n_M}$ will be rounded to integer values. As the numbers of low-mass clumps is significantly higher than the number of high-mass clumps $N_{j \neq n_M} > N_{n_M}$ due to the *clump-mass-spectrum*, Eq. 6, these rounding errors are negligible.

In general, rounding errors can always be decreased by scaling to larger surface areas and consequently larger numbers of clumps. However, we found that the error made by rounding after step c) is already negligible and therefore optimised for computing speed. Furthermore, to increase computing speed, the binomial distribution can be approximated by a Gaussian function if the expected value $\mu_j = N_j p_j$ is large. In the presented model this simplification has been used if $\mu_j > 5$.

The "superpixel" scaling is used to calculate $\langle I \rangle_{\text{ens}}$ and $\langle e^{-\tau} \rangle_{\text{ens}}$ (compare Sect. 2.3.3) as the actual pixels of area Δs^2 may eventually contain only fractions of the large clumps.

2.3.2. Voxel dependent FUV field strength

The line emissivities and opacities of the clumps contained in the voxels at different positions in the 3D model depend on the local FUV field strength. The FUV flux, coming from a known direction³, is attenuated inside the PDR.

³ Here we account for only one FUV source which is sufficient for modelling the Orion Bar PDR. However, the code can easily be extended for multiple sources.

The FUV extinction is proportional to the total hydrogen column density along the line of sight between the FUV source and the respective voxel. Röllig et al. (2013) discussed the FUV extinction in terms of the FUV-to-V color, $k_{\text{FUV}} = \langle A(\lambda)/A(V) \rangle_\lambda$, where the averaging is performed over an energy range from 6 to 13.6 eV. k_{FUV} is derived based on different grain-size distributions for the interstellar dust. For the model of the Orion Bar we adapt $k_{\text{FUV}} \approx 1.7$ based on the grain-size distribution from Weingartner & Draine (2001) for a reddening $R_V = 5.5$, the highest carbon abundance, and a constant grain volume per hydrogen⁴. Furthermore, we use the normalization for the extinction curve $A_V/N_H = 5.3 \cdot 10^{-22} \text{ cm}^2$ from Weingartner & Draine (2001).

The averaged FUV extinction caused by an individual clump $\overline{\tau_{j,\text{FUV}}}$ can be derived using the hydrogen column density from Eq. 3.

For a possible combination of clumps with different masses M_j intersecting the line of sight, i.e. a set of numbers $X = \{k_j\}_{j=1,\dots,n_M}$ with $0 \leq k_j \leq N_j$ the total FUV extinction is given by

$$\tau = \sum_{j=1}^{n_M} k_j \overline{\tau_{j,\text{FUV}}} \quad (22)$$

The probability to find this combination of clumps intersecting the line of sight is the product of binomial distributions, Eq. 21,

$$p_x = \prod_{j=1}^{n_M} B(k_j | p_j, N_j) \quad (23)$$

The *total* probability to find an FUV extinction, $\tau_{\text{tot,FUV}}$, along the line of sight is then given by the sum of the probabilities, p , of all combinations of clumps yielding the total FUV extinction $\tau_x = \tau_{\text{tot,FUV}}$. This is expressed by the sum

$$p_{\text{tot}}(\tau_{\text{tot,FUV}}) = \sum_{j=1}^{n_M} \sum_{k_j} \delta(\tau_{\text{tot,FUV}} - \tau_x) \cdot p_x \quad (24)$$

where $\delta(\dots)$ denotes the Dirac delta function and the double-sum accounts for all the possible combinations of clumps $\{k_j\}_{j=1,\dots,n_M}$ with $0 \leq k_j \leq N_j$. Eq. 24 yields values $p_{\text{tot}}(\tau_{\text{tot,FUV}})$ for each $\tau_{\text{tot,FUV}}$ which can be "assembled" from a combination of available clumps.

In principle Eq. 24 has to be evaluated for each combination, however, some combinations are highly improbable and can be neglected within the algorithm to increase computing speed. This is done by only accounting for numbers of clumps k_j which lie in a n -sigma interval around the expected value of the respective binomial distribution. Calculations presented in this paper have been performed with $n = 3$. In the presented simulations we found $\sum_{p_{\text{tot}} \neq 0} p_{\text{tot}}(\tau_{\text{tot,FUV}}) > 0.998$, confirming the low error of our approximation.

Finally, the ensemble-averaged (= voxel averaged) FUV extinction can be derived using

$$\langle e^{-\tau_{\text{FUV}}} \rangle_{\text{ens}} = \sum_{p_{\text{tot}} \neq 0} p_{\text{tot}}(\tau_{\text{tot,FUV}}) \cdot e^{-\tau_{\text{tot,FUV}}} \quad (25)$$

where $\langle \rangle_{\text{ens}}$ denotes the ensemble-averaged value. The UV attenuation in each voxel can then be described by the effective optical depth $\langle \tau_{\text{FUV}} \rangle_{\text{ens}} = -\ln(\langle e^{-\tau_{\text{FUV}}} \rangle_{\text{ens}})$.

⁴ The grain-size distribution denoted with "WD01-25" in Röllig et al. (2013) from line 25 in Table 1 in Weingartner & Draine (2001) was used.

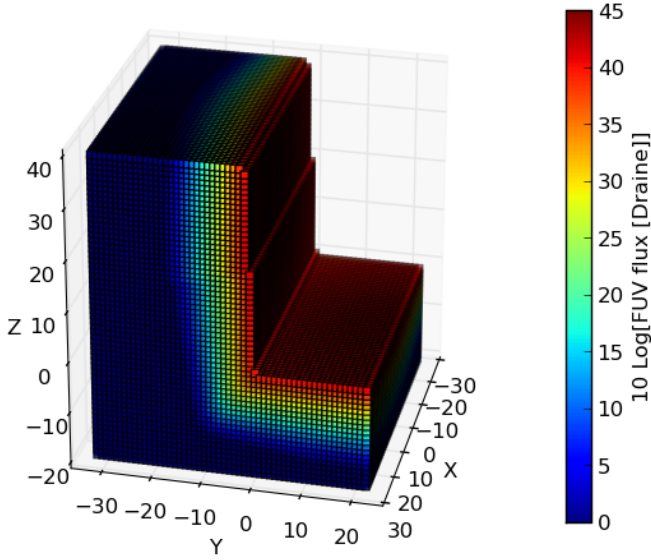


Fig. 1. A 3D compound resembling a possible geometry of the Orion Bar PDR. Each cube represents one voxel filled with at least one clumpy ensemble. The ensemble parameters can be varied between different voxels. The colour scale shows the impinging FUV flux, calculated for each voxel, for a FUV source located at [0, 22.3, 35] (Hog. 2 in Table 2). The direction to the sun corresponds to the positive z direction.

2.3.3. Ensemble averaged emissivities and opacities

Similar to the FUV extinction, we need ensemble-averaged line intensities and opacities per voxel to compute the emission of the PDR. Clump averaged line intensities \overline{I}_{cl} and opacities $\overline{\tau}_{cl}$ (compare Eqs. 4 and 5) are provided by the KOSMA- τ model. The calculation of the ensemble-averaged line intensity and opacity can be performed by the same steps as described in the last section with Eqs. 22–25 and yields

$$\langle I \rangle_{ens} = \sum_{p_{tot} \neq 0} p_{tot} (I_{tot, line}) \cdot I_{tot, line} \quad (26)$$

$$\langle e^{-\tau} \rangle_{ens} = \sum_{p_{tot} \neq 0} p_{tot} (\tau_{tot, line}) \cdot e^{-\tau_{tot, line}}. \quad (27)$$

The probabilistic approach for the calculation of the ensemble-averaged quantities, discussed here and in the previous two sections, was verified by comparison to a second method (see Appendix A).

2.3.4. Radiative transfer

In the 3D PDR simulations the geometry of the PDR is resembled using voxels having the volume $(\Delta s)^3$. To derive maps and spectra which are comparable to observations the radiative transport through the 3D model needs to be calculated. An example for a 3D set-up is shown in Fig. 1 (resembling the Orion Bar PDR, which will be introduced in Sect. 3). Each cube in Fig. 1 represents one voxel.

The radiative transfer of the UV photons is in principle just given by the extinction of the FUV flux by the sum of the optical depths $\langle \tau_{FUV} \rangle_{ens}$ in all voxels of the PDR from the FUV source to the location of interest. The resulting FUV flux is, however, a steeply changing function over the size of the voxel. Representing the voxel properties only by the flux at the voxel center thus introduces some error compared to the flux averaged over the full

volume of the voxels. In principle, this can be avoided by making the voxels small enough, but some compromise is needed to reduce the overall computational effort for the model. Therefore, we calculate the incident FUV flux at different positions within the voxels, i.e. on a 3D grid at sub-voxel scale, and average the flux at the sub-voxel gridpoints. Simulations presented in Sect. 5.1 have been performed using a $3 \times 3 \times 3$ voxel sub-grid except for the large map, Fig. 6, which has been simulated using a $5 \times 5 \times 5$ voxel sub-grid. The colour scale in Fig. 1 shows the FUV flux incident at the different voxels for the example geometry and an FUV source located at the position [0, 22.3, 25]. The emission from the clump ensemble does not require the same sub-voxel treatment as most optical depths per voxel fall below unity so that the voxel-to-voxel variation of the intensity is small.

The voxel-averaged (= ensemble-averaged) volume emissivity and absorption coefficient, $\langle \epsilon \rangle_{ens}$ and $\langle \kappa \rangle_{ens}$, are calculated based on the results from the last section:

$$\langle \epsilon \rangle_{ens} = \frac{1}{\Delta s} \langle I \rangle_{ens} \quad (28)$$

$$\langle \kappa \rangle_{ens} = -\frac{1}{\Delta s} \ln \langle e^{-\tau} \rangle_{ens} = -\frac{1}{\Delta s} \ln \left(\sum_t p_t e^{-\tau_t} \right) \quad (29)$$

where Δs denotes the depth of the voxel⁵ along the line of sight.

The velocity information of each voxel is contained in the line profiles. In the 3D PDR model we use Gaussian profiles for the emission and absorption coefficients

$$\epsilon := \langle \epsilon_v \rangle_{ens} = \langle \hat{\epsilon} \rangle_{ens} \exp \left(-\frac{(v - v_z)^2}{2\sigma^2} \right) \quad (30)$$

where v_z is the center velocity of the ensemble in the line-of-sight direction and σ the local velocity dispersion. The same profile is used for the absorption coefficients assuming complete redistribution.

The individual KOSMA- τ clumps have only a narrow velocity dispersion of $\sigma_{cl} = 0.42 \text{ km s}^{-1}$ (FWHM = 1.0 km s^{-1}), but their emission/absorption is distributed over a broader velocity range assuming a velocity dispersion between the clumps. In the Orion Bar simulations we used a fixed center velocity $v_z = 10.3 \text{ km s}^{-1}$ and dispersion of $\sigma = 1.06 \text{ km s}^{-1}$ matching the width of the optically thin ^{13}CO profiles. To simplify the notation we drop the ensemble averaging and velocity dependence in the next equations, but remind the reader that the computation is fully frequency-dependent based on the ensemble averaged quantities.

For radiation traveling into direction s the change in intensity is given by the equation of radiative transport, which, adapted for our model is

$$dI = -I\kappa ds + \epsilon ds. \quad (31)$$

Integration along a straight path length, between 0 and s , yields

$$I = \frac{1}{e^{\int_0^s \kappa dx}} \left[\int_0^s \epsilon e^{\int_0^{s'} \kappa dx} ds' + I_{bg} \right]. \quad (32)$$

For radiative transport from voxel $p-1$ to the neighbouring voxel p (Ossenkopf et al. 2001) ϵ and κ are linearly interpolated, i.e. $\epsilon := e_0 + e_1 s'$ and $\kappa := k_0 + k_1 s'$ with $s' \in [0, \Delta s]$ and with

$$\begin{aligned} k_0 &= \kappa_{p-1} \\ k_1 &= (\kappa_p - \kappa_{p-1})/\Delta s \\ e_0 &= \epsilon_{p-1} \\ e_1 &= (\epsilon_p - \epsilon_{p-1})/\Delta s \end{aligned} \quad (33)$$

⁵ Here voxels have been chosen to be cubic, i.e. having the surface area Δs^2 and the depth Δs . In general the depth of the voxel can be chosen freely.

which can be inserted into Eq. 32 yielding

$$I = \frac{1}{e^{k_0 \Delta s + \frac{1}{2} k_1 (\Delta s)^2}} \left[\int_0^{\Delta s} (e_0 + e_1 \cdot s') e^{k_0 s' + \frac{1}{2} k_1 (s')^2} ds' + I_{bg} \right]. \quad (34)$$

Eq. 34 is solved numerically and tabulated for the simulations (see Appendix B).

3. The Orion Bar PDR

The Orion Bar PDR is a prominent feature located in the Orion Nebulae (M42, NGC 1976). In observations of typical cooling lines from the UV down to radio wavelength and the IR continuum the Bar appears as a bright rim. With a distance to the Orion Nebulae of 414 ± 7 pc (Menten et al. 2007) the Orion Bar PDR is one of the nearest and hence brightest PDRs to the terrestrial observer. Consequently, a large amount of observations of the Orion Bar PDR has been performed providing us with an excellent test case for PDR models.

Chemical stratification has been observed for the Orion Bar PDR by different workgroups (van der Werf et al. 1996; van der Wiel et al. 2009; Walmsley et al. 2000). van der Wiel et al. (2009) for example discuss a layered structure with C_2H emission peaking close to the ionisation front (IF), followed by H_2CO and SO , while other species like $C^{18}O$, HCN and ^{13}CO peak deeper into the cloud.

Nowadays, it has become clear that a “simple” homogenous Bar is an insufficient description of the Orion Bar PDR. High angular resolution observations show that the Bar breaks down into substructure. We cannot list all observations that have dealt with the spatial structure of the Orion Bar. Just to name a few, Young Owl et al. (2000) presented combined single-dish and interferometric data of HCO^+ and $HCN J = 1 - 0$ which show a clumpy NE and SW Bar, Lis & Schilke (2003) showed interferometric data of the Orion Bar PDR in $H^{13}CN$ and $H^{13}CO^+$ and identify at least 10 dense condensations in the $H^{13}CN$ image, and individual clumps have also been resolved by van der Werf et al. (1996) who showed that a PDR surface can be found on each clump inside the Orion Bar.

3.1. Geometry

A common explanation for the existence of the Bar is the “Blister model”: The Orion Nebula embeds a cluster of bright and young stars which ionise their surrounding medium creating an HII -region inside the molecular cloud. At the side of the nebulae facing earth this “ HII -bubble” has broken out of the cloud, enabling observations of the cavity and of the Orion Bar PDR which forms one of the edges of the cavity, illuminated by the strong FUV radiation from the young star cluster (see for example Wen & O’dell 1995 and references therein).

The dominating ionising source and most massive star is Θ^1 Ori C which produces $\sim 80\%$ of the H -ionising photons. Θ^1 Ori D, the second most massive star of the “Trapezium” system, accounts for another $\sim 15\%$ (Draine 2011). The IF, as marked for example by the peak position of the OI or $[FeII]$ emission (Walmsley et al. 2000), $[SiII]$ (Pellegrini et al. 2009), or $[NII]$ (Bernard-Salas et al. 2012) is located at $111''$ (corresponding to 0.223 pc) projected distance from Θ^1 Ori C.

The flux at the IF has been estimated to correspond to an enhancement over the average interstellar radiation field of a factor $\approx 4.4 \cdot 10^4 \chi_0$ (Hogerheijde et al. 1995; Jansen et al. 1995). We have verified that this value lies in a probable range (see Appendix C).

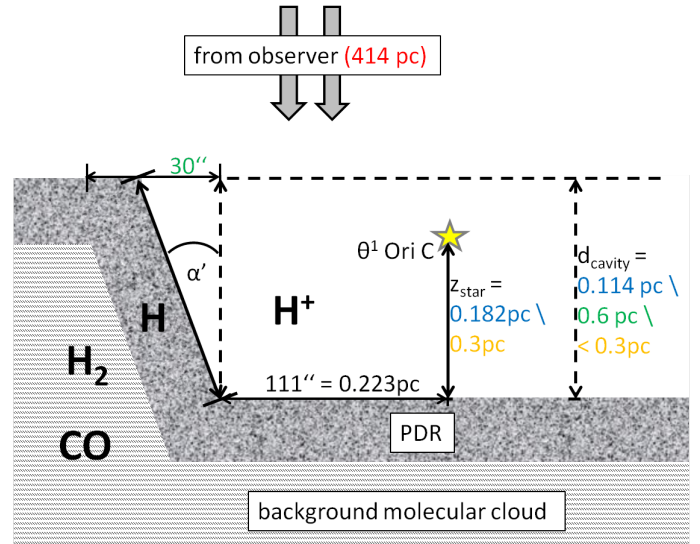


Fig. 2. “Face-on to edge-on to face-on” Orion Bar Geometry as proposed by Hogerheijde et al. (1995). Values are taken from: green: Hogerheijde et al. (1995); red: Menten et al. (2007); blue: Pellegrini et al. (2009); and orange: van der Werf et al. (2013). For the inclination angle, α' , values between 3° and 15° have been discussed (Melnick et al. 2012).

Different geometries have been proposed to model the Orion Bar, the dominating idea is a slightly inclined face-on / edge-on / face-on geometry first introduced by Hogerheijde et al. (1995) and Jansen et al. (1995). Many other workgroups have used adaptations of this geometry to model the observations (see e.g. Pellegrini et al. 2009). A schematic picture of this geometry is shown in Fig. 2. Due to the increased column density along the line of sight, this geometry naturally explains the observed intensity peak.

The depth of the cavity, the inclination angle of the Bar (α' , not to be confused with the power-law exponent α from Eq. 6) and the “z-position” (position on the line of sight to the observer) of the illuminating cluster have been subject to discussions. Different possibilities are indicated in Fig. 2.

This geometry is consistent with all the FIR and submm observations, but an indication that this geometry needs at least some modifications stems from optical observations (McCaughrean 2002) that show some shadowing at the very edge of the Orion Bar. This would be explained by a configuration where the Orion Bar is not the edge of a cavity but rather a filament as proposed by Walmsley et al. (2000); Arab et al. (2012). This can be modelled using a cylindrical shape.

3.2. Observations

Due to the tremendous amount of data available for the Orion Bar PDR we need to make a selection. As the aim of this paper focuses on the description and the testing of the 3D PDR model, we selected only observations of abundant and simple species: CO isotopes, HCO^+ and the $[CII]$ cooling line. An expansion including many more species is of course possible.

We use $[CII]$, CO 10-9, CO 16-15, ^{13}CO 5-4, ^{13}CO 10-9 and HCO^+ 6-5 line observations of the Orion Bar PDR observed with the Heterodyne Instrument for the Far-Infrared (HIFI, de Graauw et al. 2010) on-board the *Herschel* Space Observatory (Pilbratt et al. 2010). The observations have been performed as part of the EXtra-Ordinary Sources (HEXOS) guaranteed-time

key program (Bergin et al. 2010). Combined with low- J CO and HCO^+ rotational lines (see below) these lines are well suited to trace the chemical stratification observed in the Orion Bar PDR.

All presented HIFI/*Herschel* observations are strips across the Bar with a width of $1'$ or more, except for the CO 16-15 observations where a single cut has been observed. The observations have been taken in the on-the-fly (OTF) observing mode around the center position ($\alpha_{J2000} = 5^h35^m20.81^s$, $\delta_{J2000} = -5^\circ25'17.1''$) with a position angle perpendicular to the Bar, i.e. 145° east of north, and an OFF position 6 arcminutes southeast of the map. The observations used the Wide-Band-Spectrometer (WBS) with a frequency resolution of 1.1 km s^{-1} . Both polarizations were averaged to improve the signal-to-noise ratio. Integration times varied between 4 and 30 s resulting in noise levels between a 0.02 and 0.3 K. The high-frequency HIFI/*Herschel* data, i.e. the maps of [CII] and CO 16-15 have been reduced in HIPE as described by Ossenkopf et al. (2013). All other lines were analysed using the GILDAS software⁶ for baseline subtraction and spatial resampling. An overlay of our data, [CII] overplotting ^{13}CO 10-9, is shown in Fig. 3.

The line intensities (Table 1) are given here on a T_{mb} scale. For the HIFI/*Herschel* observations T_{mb} is a factor 1.26 to 1.5 higher than T_A^* , depending on the respective frequency (Roelfsema et al. 2012). As discussed by Ossenkopf et al. (2013), the scaling from T_A^* to T_{mb} is questionable for very extended emission (like [CII]) where the error beam of the telescope is likely to be filled with emission of approximately the same brightness as the main beam. Hence, for extended emission our intensities are upper limits.

Our data set is combined with ground-based observations of CO 2-1, CO 3-2, CO 6-5, ^{13}CO 3-2, ^{13}CO 6-5 and HCO^+ 3-2 observed with the Caltech Submillimeter Observatory (CSO) (D. Lis, priv. comm.). The CSO observations are typically more extended but overlap with the HIFI/*Herschel* maps. To facilitate the comparison between the maps, the reference positions of all maps have been shifted to be equal to the CSO reference position ($5^h35^m20.122^s$, $-5^\circ25'21.96''$).

To simplify the analysis of the stratification profile, the maps have been rotated around the CSO reference position by -145° (-145° clockwise), resulting in an orientation of the Orion Bar parallel to the “ x -axis” (compare Figs. 3 and 4). As we focus on the stratification of the chemical and excitation structure across the Orion Bar, the observed spectra have been averaged along rows of pixels parallel to the x -axis ensuring that we average over clumps and interclump medium. In the x -range between $-11.3''$ and $-43.5''$ the Orion Bar has a very straight appearance in all of our maps and an average over $\sim 30''$ guarantees that we are not affected by individual clumps, but consider a clump-ensemble on the observational side as well (see Sect. 4)⁷.

Gaussian profiles were fitted to the averaged spectra. We fit two Gaussian profiles, one profile fixed at a centre velocity of 8 km s^{-1} to exclude the emission from the Orion Ridge (van der Tak et al. 2013). The other profile fits the main component at about 11 km s^{-1} originating from the Orion Bar. Integration of this component yields the line integrated intensity, averaged for the respective row (y -position). The peak position was determined by fitting a parabola to the row-averaged intensities at the different y -positions. As deviations between the fitting points and the fitted parabolas are very small, we assume the pointing error of the telescope as the main uncertainty in the determination of the peak position. These are $2.4''$ for HIFI/*Herschel*

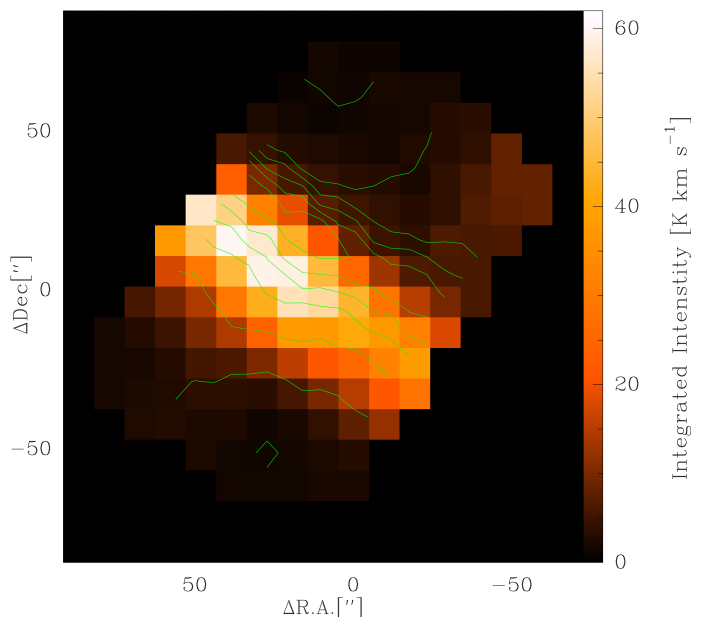


Fig. 3. The Orion Bar observed with HIFI/*Herschel*. The green contours show [CII] line intensities integrated between 7 and 13 km s^{-1} . The contours range between 200 and 800 K km s^{-1} in steps of 100 K km s^{-1} . The colour scale gives the ^{13}CO 10-9 line intensity, integrated between 9 and 12 km s^{-1} . The reference position is the “CSO reference position”, ($5^h35^m20.122^s$, $-5^\circ25'21.96''$).

(Pilbratt et al. 2010) and $3''$ for CSO data⁸. The resulting peak intensities and y -offsets are summarised in Table 1 for the different transitions.

4. 3D Model of the Orion Bar PDR

We have composed the 3D model of the Orion Bar from cubic voxels with a size of 0.01 pc , corresponding to $5.0''$ at the distance of 414 pc . The voxel size is small enough to analyse stratification effects but large enough to ensure that the total number of voxels can be treated on a standard PC. Our Cartesian coordinate system is chosen in such a way that the x -direction is parallel to the Orion Bar and the z -direction points towards the observer. As we are mainly interested in the stratification of the Orion Bar here, the current model ignores any variation of the density structure in x -direction. This reduces the number of free parameters, but excludes for the moment the simulation of additional structures like the Orion ridge.

Two fundamentally different geometries have been tested for the Orion Bar PDR. The first one is the geometry discussed by Hogerheijde et al. (1995) (see Figs. 1 and 2) consisting of an almost edge-on cavity wall facing the illumination from $\Theta^1 \text{ Ori C}$. In this model, we have varied the inclination angle (α' in Fig. 2) and the depth of the cavity ($\approx 0.6 \text{ pc}$ in Hogerheijde et al. 1995). The second geometry is the filament model proposed by Walmsley et al. (2000); Arab et al. (2012) consisting of a cylinder in the plane of the sky with the main symmetry axis along the Bar (see Fig. 5). As a first test of this geometry, we adopted the same diameter of the cylinder as used for the cavity depth (0.6 pc).

The main illuminating source $\Theta^1 \text{ Ori C}$ is $111''$ away from the interface. This corresponds to a separation by 22.3 voxels in y -direction between star and interface. In x direction, the location of the star defines our zero point, i.e. $\Theta^1 \text{ Ori C}$ is located

⁶ <http://www.iram.fr/IRAMFR/GILDAS>

⁷ For the CO 16-15 cut, each “row” only contains one pixel

⁸ <http://cso.caltech.edu/wiki/cso/science/overview>

Table 1. Summary of averaged integrated intensities and spatial offsets of the observations.

Species	Frequency ^a [GHz]	Observatory	Beamsize ^b [arcsec]	Peak intensity ^c [K km s ⁻¹]	y-offset ^d [pc]	y-offset ^d [arcsec]	Δy_{obs}^e [pc]
[CII]	1900.5369	HIFI/Herschel	11.2	1153	-0.016 ± 0.005	-7.8 ± 2.4	0
CO 2-1	230.5380000	CSO	30.5	402	0.029 ± 0.006	14.6 ± 3.0	0.045 ± 0.008
CO 3-2	345.7959899	CSO	21.9	405.9	0.014 ± 0.006	7.2 ± 3.0	0.030 ± 0.008
CO 6-5	691.4730763	CSO	10.6	560	0.020 ± 0.006	9.8 ± 3.0	0.036 ± 0.008
CO 10-9	1151.985452	HIFI/Herschel	18.4	374	0.021 ± 0.005	10.5 ± 2.4	0.037 ± 0.007
CO 16-15	1841.345506	HIFI/Herschel	11.5	128	0.019 ± 0.005	9.4 ± 2.4	0.035 ± 0.007
¹³ CO 3-2	330.5879653	CSO	21.9	114	0.026 ± 0.006	12.8 ± 3.0	0.042 ± 0.008
¹³ CO 5-4	550.9262851	HIFI/Herschel	38.5	120	0.042 ± 0.005	20.8 ± 2.4	0.058 ± 0.007
¹³ CO 6-5	661.0672766	CSO	10.6	157	0.030 ± 0.006	14.8 ± 3.0	0.046 ± 0.008
¹³ CO 10-9	1101.3495971	HIFI/Herschel	19.3	92	0.018 ± 0.005	9.0 ± 2.4	0.034 ± 0.007
HCO ⁺ 3-2	267.5576259	CSO	30.5	46	0.010 ± 0.006	5.0 ± 3.0	0.026 ± 0.008
HCO ⁺ 6-5	535.0615810	HIFI/Herschel	39.6	8.7	0.022 ± 0.005	11.2 ± 2.4	0.038 ± 0.007

Notes. ^(a) Taken from “The Cologne Database for Molecular Spectroscopy (CDMS)” (Müller et al. 2001, 2005; <http://www.astro.uni-koeln.de/cdms/>) ^(b) Calculated based on Roelfsema et al. (2012) for HIFI/Herschel. Taken from <http://www.submm.caltech.edu/cso/receivers/beams.html> “calculated FWHM” for CSO data. For non-circular beams an average has been used. ^(c) Line integrated intensity averaged along the Bar at the position of the peak (see text), T_{mb} scale ^(d) Measured spatial offset into the PDR (with position angle 145° east of north) relative to the CSO reference position. ^(e) Measured spatial shift into the PDR (with position angle 145° east of north) relative to the [CII] peak position.

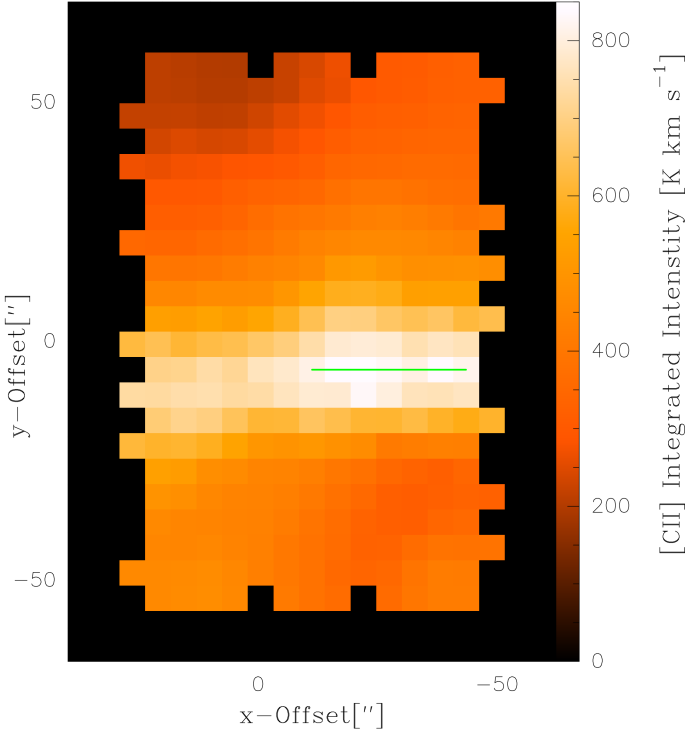


Fig. 4. [CII] integrated intensity (same as the contours in Fig. 3) rotated by -145° , i.e. Θ^1 Ori C in the north-west of the Bar is at the bottom in this orientation. The green line marks the cut with the highest averaged line integrated intensity, including all pixels with x-offsets between $-11.3''$ and $-43.5''$.

at $[0, y_{\text{IF}} + 22.3, z_{\text{star}}]$ in the model. We varied the z position of the star (z_{star}) to obtain the best fit. We started with a position of the illuminating source, z_{star} at half of the depth of the cavity. However, a position with a significant depth in the cavity always produces cooler material, exposed to a lower FUV field, at the edge of the Orion Bar facing the observer (compare Fig. 9). This shows up as foreground absorption in the FIR lines and continuum, which is not observed for the Orion Bar. Hence, we had to

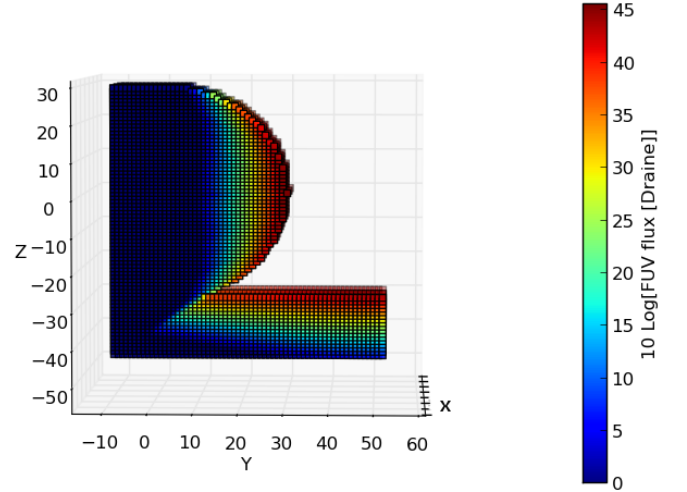


Fig. 5. Cylindrical Orion Bar model. The colour scale gives the incident FUV flux for each voxel as in Fig. 1. For this plot the illuminating star Θ^1 Ori C is located at $[0, 52.3, 0]$.

switch to a z positions of the stars close to the edge of the cavity. In all “Hogerheijde models” we place Θ^1 Ori C five voxels (0.05 pc) below the upper edge of the cavity. In the cylindrical geometry there is, however, less foreground that would shadow the illuminated edge. Here, the star is placed at the height of the center of the cylinder. A placement deeper in the cavity is excluded by the lack of foreground absorption, a placement close to the upper edge of the cylinder would give the same behaviour as the tilted bar in the “Hogerheijde” setup, not providing any additional information.

The flux from Θ^1 Ori C has been estimated in Appendix. C to fall between $0.63 \cdot 10^4 \chi_0$ and $13.8 \cdot 10^4 \chi_0$. In the simulations it quickly turned out that values below $2 \cdot 10^4 \chi_0$ are too weak to excite some of the species originating from the dense clumps. Especially CO 16-15 and HCO⁺ 6-5 could not be reproduced at all with such values. For all further computations we thus stuck to the fixed value of $4.4 \cdot 10^4 \chi_0$ proposed by Hoger-

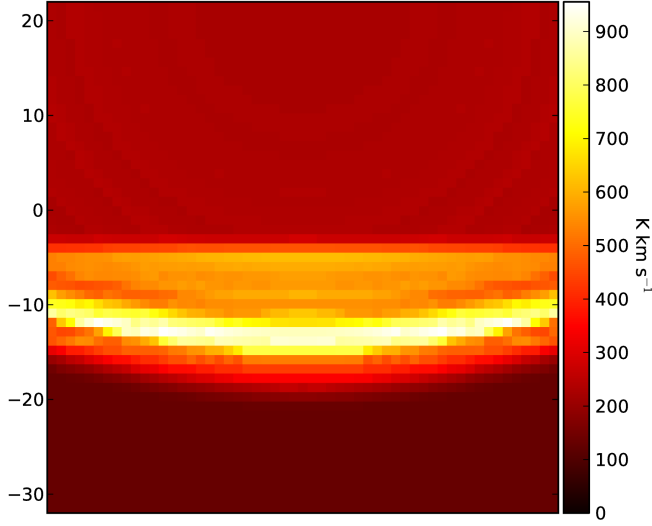


Fig. 6. Simulated map of line-integrated CO 3-2 emission of the Orion Bar PDR, based on a model similar to “Hog. 2” (see Table 2). The coordinates are given in pixels where one pixel corresponds to 0.01 pc or 5” on the sky. The illuminating star Θ^1 Ori C is located outside of the map on the top.

heijde et al. (1995) that falls well within the possible range. This high flux value also implies that the FUV absorption inside the HII region between star and PDR is basically negligible in agreement with the lack of dust observed in the cavity. Dust must have been blown out by the strong stellar winds.

Hogerheijde derive a total H_2 column density of $N_{H_2} = 6.5 \times 10^{22} \text{ cm}^{-2}$ along the line of sight (peak) for a path length of 0.6 pc. For a constant density along the line of sight this translates into $n_{H_2} = N_{H_2}/(0.6 \text{ pc}) = 3.5 \times 10^4 \text{ cm}^{-3}$. Consequently, the total mass in a voxel with volume $(0.01 \text{ pc})^3$ is:

$$\begin{aligned} M_{\text{voxel}} &= 3.5 \times 10^4 \text{ cm}^{-3} m_{H_2} \left(\frac{3.086 \times 10^{18} \text{ cm}}{\text{pc}} \right)^3 (0.01 \text{ pc})^3 \\ &= 0.00173 M_{\odot} \end{aligned} \quad (35)$$

that we use as baseline for all our simulations.

The clump ensembles in the models contain masses from $10^{-3} M_{\odot}$ to $10^0 M_{\odot}$. The upper limit matches the clump masses in the range 0.5-1.5 M_{\odot} determined by Lis & Schilke (2003) based on the measured line widths and the virial theorem. The exact value of the lower mass limit is not critical as we found that it has very little impact on the ensemble emissivities because of the small mass contained in those clumps (see Sect. 2.2.1).

The thin interclump medium was mimicked by a second clump ensemble with a factor 100 lower density. It consists only of clumps with mass of $10^{-2} M_{\odot}$ that fill the space between the dense clumps.

The model allows for the simulation of full maps. Fig. 6 shows a map of CO 3-2 intensities for model similar to model “Hog. 2” from Table 2. We find a combination of the imprint of the flat density structure and a curvature stemming from the varying distance to the illuminating star. Fig. 7 shows the same map after convolution with a Gaussian beam of 22” FWHM matching the CSO beam used in the observations. It blurs some of the detailed structures, but still allows to recover the stratification of the emission in the Bar.

For the systematic parameter study, we reduced the map size to a strip of three pixels x -extension across the Orion Bar only and skipped the beam convolution. This cuts enables us to gain

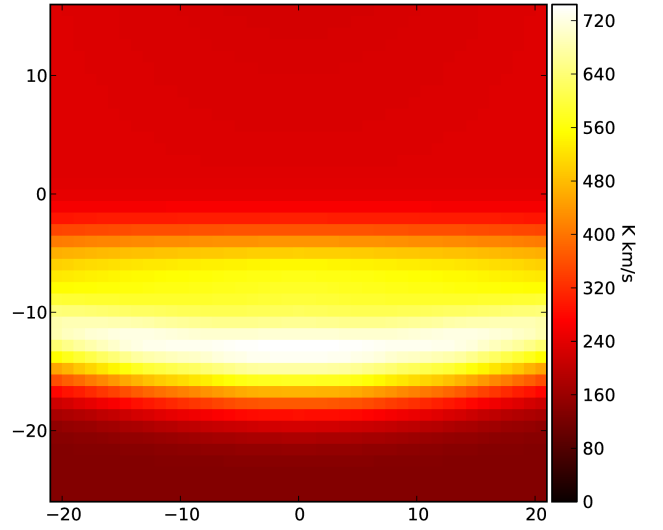


Fig. 7. Same as Fig. 6 but after convolution with a Gaussian beam of 22” or 4.4 pixels FWHM (see Table. 1).

the full information concerning peak integrated intensities and peak offsets within short computing time (a few hours). Typical simulation results are shown in Fig. 8 based on model “Hog. 1”.

5. Parameter scans

5.1. Model runs

The total number of free parameters in our 3D model is still huge and we performed tests with many parameter combinations. Here, we can only present a few of them starting from our a posteriori knowledge of the best fitting model (“Hog. 1”, Fig. 8) where we discuss the impact of the different parameters. The different geometries and parameter sets for the Orion Bar PDR are summarised in Table 2. The first 12 rows in Table 2 give different parameter sets in the context of the “Hogerheijde” model, while the last row refers to the cylindrical model (compare Sect. 4 and Figs. 1 and 5).

To evaluate the goodness of the fit, with respect to the simultaneous reproduction of the integrated line intensities and the Orion Bar stratification structure, we determine the position and the integrated intensity of the pixel with the highest integrated intensity for each transition from our model strips.

The stratification is measured in terms of the y -offset of the peak intensity of each line relative to the [CII] peak position: $\Delta y_i = y_i - y_{[\text{CII}]}$ (negative signs mean a shift in the direction towards Θ^1 Ori C, see Table 1). Simulations and observations are compared by deriving the difference between the offsets

$$y_{\text{diff}} = \Delta y_i - \Delta y_{\text{obs}} \quad (36)$$

(by definition, $y_{\text{diff}} = 0$ for [CII], our reference coordinate). The relative differences in peak integrated intensity between simulation and observation are computed as $I_{\text{rel}} = I_{\text{fit}}/I_{\text{obs}}$ and all deviations of intensities and offsets for the different models are summarised in Figs. 10 through 13. This approach yields a clear way to compare and evaluate the different models and to identify systematic behaviour. In a few cases the low- J CO and ^{13}CO transitions show multiple peaks (see for example ^{13}CO 3-2 in Fig. 8). In this case our method detects the stronger peak. However, as these cases are limited to a few. In most cases the two peaks are separated by at least 7 pixels (0.07 pc or 35”, compare

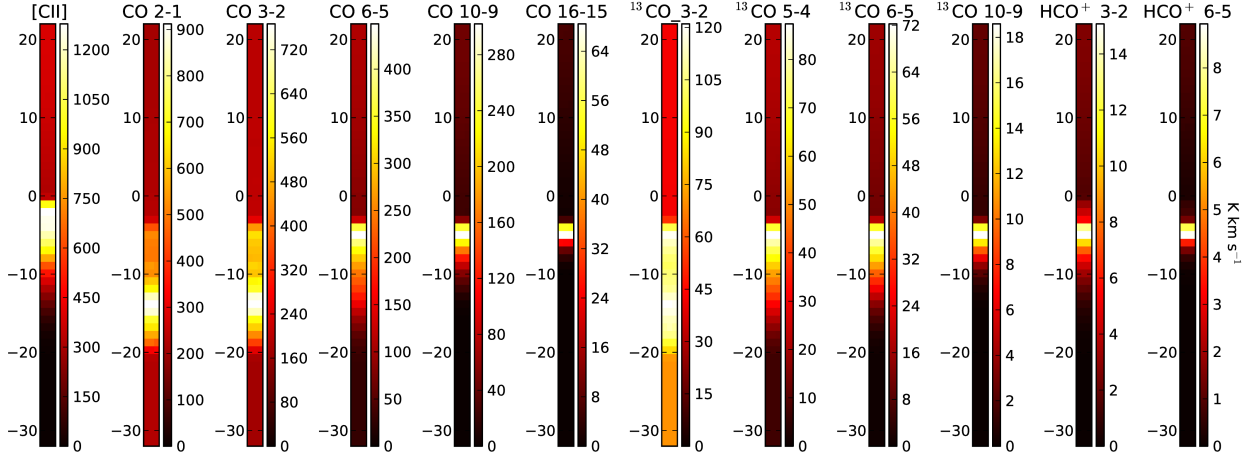


Fig. 8. Simulated cuts (three pixel wide) perpendicular to the Orion Bar, based on model “Hog. 1” from Table 2. The colour scales give the line integrated intensities in K km s⁻¹ for the transitions indicated above the respective plot.

Table 2. Models with different geometries and parameters tested for the Orion Bar PDR

Name	ρ_{ens} [cm ⁻³]		clump mass fraction ^a	clump depth [pc]	α' [deg]	d_{cavity} [pc]
	clumps	interclump				
Hog. 1	$4 \cdot 10^6$	$4 \cdot 10^4$	0.816	0.03	3	0.3
Hog. 2	$4 \cdot 10^6$	$4 \cdot 10^4$	0.816	0.03	15	0.3
Hog. 3	$4 \cdot 10^6$	$4 \cdot 10^4$	0.816	0.03	0	0.3
Hog. 4	$4 \cdot 10^6$	$4 \cdot 10^4$	0.816	0.03	3	0.4
Hog. 5	$4 \cdot 10^6$	$4 \cdot 10^4$	0.816	0.03	3	0.6
Hog. 6	$4 \cdot 10^6$	$3 \cdot 10^4$	0.816	0.03	3	0.3
Hog. 7	$4 \cdot 10^6$	$5 \cdot 10^5$	0.816	0.03	3	0.3
Hog. 8	10^6	$4 \cdot 10^4$	0.816	0.03	3	0.3
Hog. 9	$4 \cdot 10^6$	$4 \cdot 10^4$	0.667	0.03	3	0.3
Hog. 10	$4 \cdot 10^6$	$4 \cdot 10^4$	0.875	0.03	3	0.3
Hog. 11	$4 \cdot 10^6$	$4 \cdot 10^4$	0.816	0.04	3	0.3
Hog. 12	$4 \cdot 10^6$	$4 \cdot 10^4$	0.816	0	3	0.3
Cyl.	$4 \cdot 10^6$	$3 \cdot 10^4$	0.816	0.03	-	0.6

Notes. Rows 1 to 12 refer to the “Hogerheijde” geometry, while the last column refers to the cylindrical model. The 6th column indicates a homogeneous model, all other models utilise a density profile. α' gives the inclination angle of the Bar (which is not needed in the cylindrical model), d_{cavity} refers to the depth of the cavity and z_{star} gives the z -position of the star in the respective coordinate system. Note that the coordinate system is different for the cylindrical model (see Fig. 5). ^(a) Ratio of the mass in the dense clump ensemble over the total mass including the interclump medium. The total mass in the voxels is $0.00424 M_{\odot}$.

Fig. 8 or Figs. 10 and 12). As the maximal beamsize for the low- J CO and ¹³CO transitions is about 22″, convolution with the beam would still leave the two peaks distinguishable.

In the next subsection we discuss the effect of systematic changes of some of the PDR parameters on the fitting results for the “Hogerheijde” model. In addition to the cavity geometry we tested a model with a cylindrical geometry with the parameters indicated in the last row of Table 2.

The best fits to the observed properties are provided by the cavity models “Hog. 1” and “Hog. 3” which are very similar (differences between these models will be discussed below). The stratification profile is reproduced within 0.03 pc by both models (compare Fig. 10) except for the low- J CO and ¹³CO transitions which turn out to be problematic (see below). The peak integrated intensities show some scatter around the observed values (the models somewhat underestimates the high- J ¹³CO transitions, CO 16-15, and HCO⁺ 3-2. The CO 2-1 and 3-2 intensities are about a factor two too high), but all intensities are re-

produced within a factor 2 (compare Fig. 11). In the following model “Hog. 1” will be used as a reference for the parameter variations (first row of Table 2).

5.2. Results

Inclination angle: As summarised in Table 2 we test models with α' equal to 0, 3 or 15 deg in models “Hog. 3”, “Hog. 1” and “Hog. 2” respectively. As shown in Fig. 11 the line intensities for the different transitions increase with lower inclination angles. This is especially visible for the species which emit very locally (compare Fig. 9). For these species a non-inclined Bar provides significantly more column density along one line of sight. For wider distributed transitions the effect is less visible. In terms of stratification the 0 and the 3 deg inclined Bar show a very similar behaviour, except for ¹³CO 3-2. The huge difference in the y -offset for this transition is due to the fact that the ¹³CO 3-2 cut shows a double-peak profile (compare Fig. 8). For the chosen

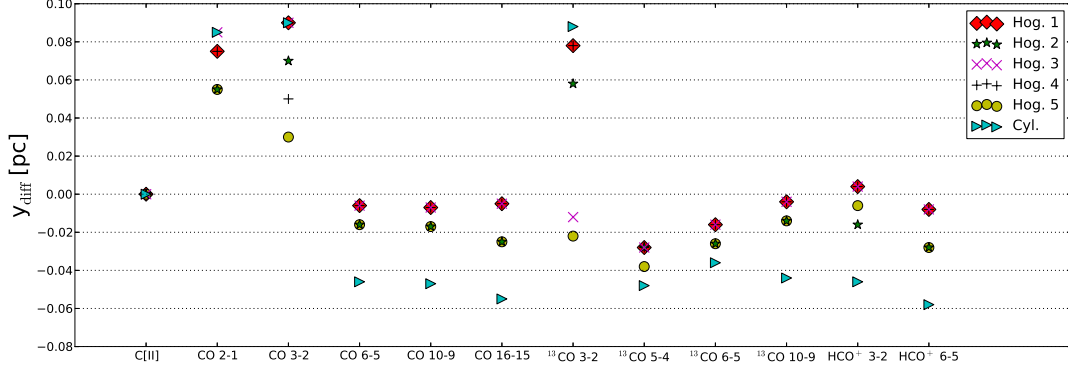


Fig. 10. Deviation of the y-offsets of the peak positions between simulations and observations as defined in Eq. 36 for the reference model “Hog. 1” and models “Hog. 2”–“Hog. 5.”. In addition, the cylindrical model is shown. All offsets are relative to the [CII] peak position. For the reference transitions, [CII], y_{diff} is always zero. Different transitions and models (see Table 2) are indicated in the plot.

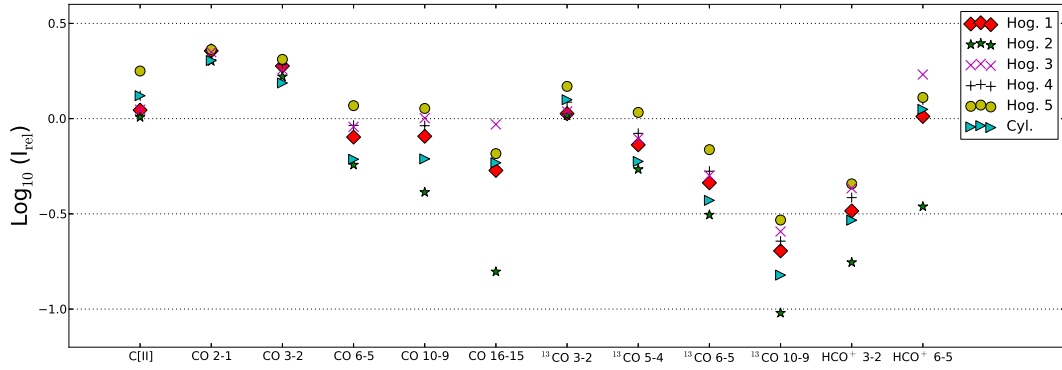


Fig. 11. Deviation of the simulated peak integrated intensity from the observed intensity, $I_{\text{rel}} = I_{\text{fit}}/I_{\text{obs}}$, for the same models as in Fig. 10.

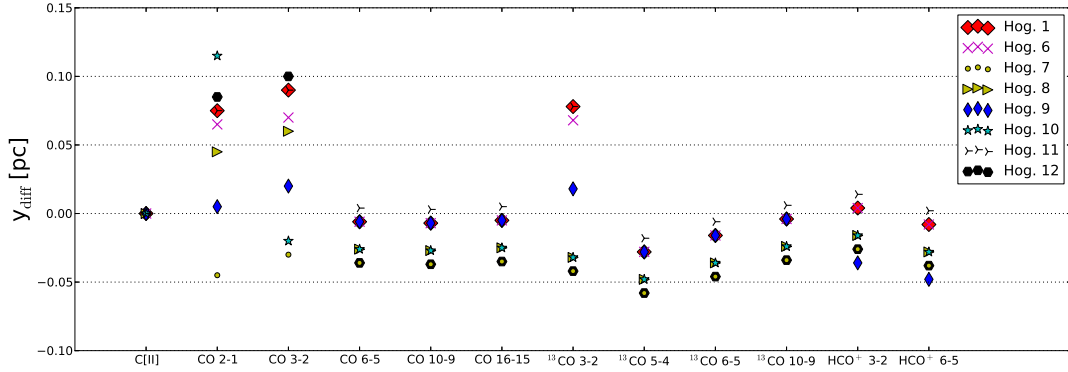


Fig. 12. Deviation of the y-offsets of the peak positions between simulations and observations as defined in Eq. 36 for the reference model “Hog. 1” and models “Hog. 6”–“Hog. 12.”. In addition, the cylindrical model is shown. All offsets are relative to the [CII] peak position. For the reference transitions, [CII], y_{diff} is always zero. Different transitions and models (see Table 2) are indicated in the plot.

parameters both peaks are of similar strength, for model “Hog. 1” the peak deep inside the PDR is somewhat stronger, while for model “Hog. 5” the stronger peak is closer to the IF. As our method only detects the strongest peak, the offsets are very different. In terms of line intensities models “Hog. 1” and “Hog. 5” also show similar trends, however, model “Hog. 5” reproduces the high- J CO and ^{13}CO lines and HCO^+ 3-2 somewhat better, while model “Hog. 1” is more exact in the reproduction of HCO^+

6-5. For model “Hog. 4” the y-offset is systematically smaller for nearly all transitions which is probably due to the fact the for the strongly inclined Bar also the [CII] peak, which is our reference position, is shifted 0.08 pc into the PDR where column densities are higher, reducing the offset relative to the other transitions. Furthermore, for most transitions the column density is not sufficient to produce the observed line emissions. We conclude that we cannot distinguish whether the 0 or the 3 deg inclined model

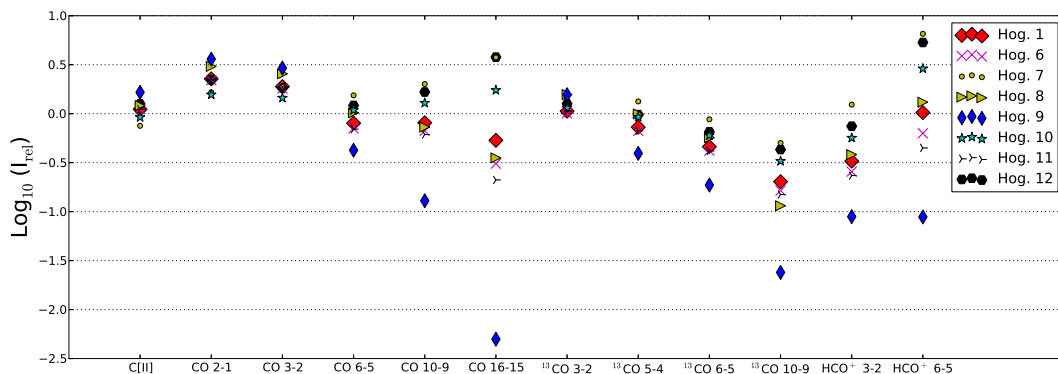


Fig. 13. Deviation of the simulated peak integrated intensity from the observed intensity, $I_{\text{rel}} = I_{\text{fit}}/I_{\text{obs}}$, for the same models as in Fig. 12.

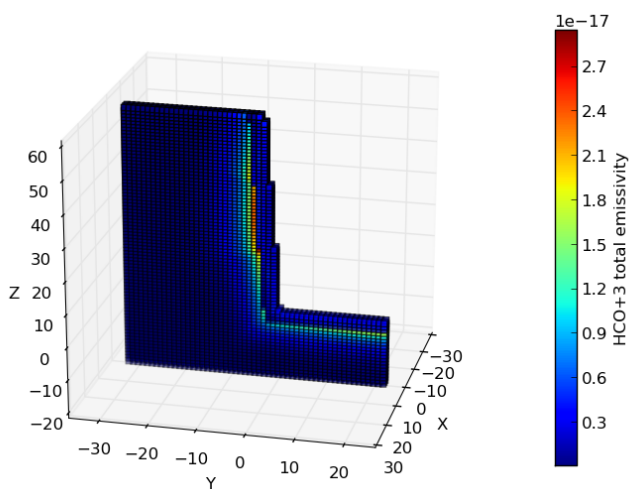


Fig. 9. Volume emissivity in $[K \text{ km s}^{-1} \text{ cm}^{-1}]$ of $\text{HCO}^+ 3-2$ for a cut through the Bar. The geometry is based on model “Hog. 5”, but with the illuminating source located at $[0, 22.3, 30]$. HCO^+ is found to emit very locally inside the PDR, hence, for this position of the star, cold foreground material is found along the line of sight.

is in favour, but we can rule out the 15 deg model in terms of line intensities and stratification.

Depth of the cavity: In the next step we vary the depth of the cavity, and therefore the length of the line of sight through the Bar. We have used 0.6 pc (see Hogerheijde et al. 1995), 0.4 pc and 0.3 pc (models “Hog. 5”, Hog. 4” and “Hog. 1” respectively, where all other parameters are kept constant). Models “Hog. 1” and “Hog. 4” behave identical in terms of stratification, except for CO 3-2. For model “Hog. 5” the y-offsets are reduced for all transitions. This is probably due to the fact that the reference [CII] peak is shifted further into the PDR. In general the line intensities for the different transitions increase with increasing column density. This effect is reduced for CO 16-15 and $\text{HCO}^+ 6-5$. The emission of these transitions is spatially strongly peaking close to illuminating source, i.e. it is localized at the same z -position as $\Theta^1 \text{ Ori C}$. Therefore their emission is almost independent of the total column density of gas. Other transitions, especially [CII] and the low- J CO and ^{13}CO lines, have an extended emission so that their line intensities decrease for a shallower cavity with less column density. However, the effect is damp-

ened for CO 2-1 and CO 3-2 which are saturated. Overall, the three models are equally well-fitting in terms of line intensities. However, model “Hog. 5” fails in reproducing the stratification for nearly all transitions and is therefore less favourable.

Mass per voxel: Each voxel contains the same amount of interclump medium. For voxels at some depth into the PDR (compare Table 2) dense clumps have been added to the interclump medium. The extinction of the FUV flux depends on the mass per voxel and on the ensemble-averaged densities. Lower ensemble-averaged densities, which imply a more homogeneous distribution of the mass cause stronger FUV extinction. For the same reason, the FUV extinction is dominated by the thinner interclump medium. Hence, varying of the interclump mass per voxel and the average density of the interclump medium can be used to fine-tune the FUV penetration depth. In addition, the interclump medium has to account for a large fraction of the [CII] emission and partly for the low- J HCO^+ , CO and ^{13}CO lines. Dense clumps are added to the interclumps medium to provide sufficient emission of the high- J CO and ^{13}CO lines, and partly of HCO^+ . We find that the values derived based on Hogerheijde et al. (1995), i.e. $0.00173 M_{\odot}$ per pixel and 10% of the material in clumps cause to strong FUV extinction and to weak line intensities of the high-density tracers. An interclump mass per pixel of $0.45 \times 0.00173 M_{\odot}$ causes less FUV extinction, allowing for some transitions to peak in 0.03 pc depth, and provides sufficient [CII] emission. A large fraction of mass in clumps ($2 \times 0.00173 M_{\odot}$) has to be added at the position of the clump ridge, to provide sufficient emission of the transitions originating from high-density regions. The resulting total mass of $0.00424 M_{\odot}$ per voxel has been fixed. Variations in the ratio between clumps and interclump medium are discussed below.

Density of the interclump medium: The interclump medium has to account for the [CII] emission and partly for the emission of other transitions. Furthermore, fine-tuning of the interclump mass per pixel and density is necessary to provide reasonable FUV extinction. We show two examples for the behaviour of the interclump medium: in model “Hog. 6” the density of the interclump medium has been reduced to $3 \times 10^4 \text{ cm}^{-3}$ (compared to $4 \times 10^4 \text{ cm}^{-3}$ in all previous models). Models “Hog. 1” and “Hog. 6” have identical parameters, except for the interclump density. Due to the stronger FUV extinction in model “Hog. 6” the y-offsets for the tracers that peak deep inside of the cloud, mainly the low- J CO transitions, are reduced compared to

“Hog. 1” model. The intensities of some transitions, especially the ^{13}CO transitions and HCO^+ 3-2 are underestimated by model “Hog. 1”. This effect becomes worse for model “Hog. 6” for the line intensities of all transitions peaking at about 0.03 pc (4th row of voxels) into the PDR, where the inset of clumps begins. Only $[\text{CII}]$, peaking at the surface, is hardly affected as well as the low- J CO and ^{13}CO transitions, which peak at larger depth into the PDR where they find their “ideal” FUV field. As a second example, in model “Hog. 7” the density of the interclump medium has been increased to $5 \times 10^5 \text{ cm}^{-3}$. This model can be directly ruled out, as due to the low FUV extinction all species peak at the same depth (0.05 pc) into the PDR marking the reproduction of a stratification profile impossible. We conclude that within this comparison model “Hog. 1” provides the best fit, but differences between model “Hog. 1” and model “Hog. 6” are small.

Mass fraction of dense clumps: For the total clump mass per voxel we started with a small fraction of the total “Hogerheijde mass”, 0.00173 M_{\odot} per voxel, which was also not sufficient for reproducing the emission, hence, the mass was increased stepwise. Here, we present models with three different clump/interclump mass ratios. In the reference model “Hog. 1” the ratio between the mass contained in clumps and the total mass contained in the voxels is 0.816. Model “Hog. 9” and model “Hog. 10” have different ratios of 0.677 and 0.875, respectively. The total mass per voxel was kept constant (0.00424 M_{\odot} per voxel). In model “Hog. 9”, which has most interclump medium, the FUV extinction is a lot too strong. This has two effects: first, species peaking inside the cloud, at 0.03 pc where the ridge of dense clumps begins, are not sufficiently excited. For example, CO 16-15 emission, which needs high densities and sufficient FUV excitation, is more than two orders of magnitude too weak. A second effect is that the HCO^+ emission cannot be excited at 0.03 pc depth. Hence, the peak is shifted close to the IF where only interclump medium is present. Consequently, HCO^+ emission is found to be a lot too weak an actually peaks in front of the $[\text{CII}]$ peak. We conclude that the amount of interclump medium needs to be decreased. Model “Hog. 10” contains more clumps and less interclump medium compared to the reference model. The result is that, except for CO 2-1, the y-offsets become too small (due to the low FUV extinction the $[\text{CII}]$ peak is shifted 0.04 pc into the PDR and the other transitions peak 0.05 pc behind the IF). In addition, it needs to be mentioned that model “Hog. 10” is the only “Hogerheijde” model that overestimates CO 16-15 and HCO^+ 6-5 due to the strong FUV field at the depth of the clump ridge. Still, our reference model is the only model which can provide acceptable values for line intensities and stratification.

Clump ensemble density: For the ensemble-averaged density of the dense clumps we started with 10^6 cm^{-3} . However, this density (here represented by model “Hog. 8” from Table. 2) has several disadvantages. First, clumps with density 10^6 cm^{-3} are found to contribute to the $[\text{CII}]$ emission and therefore tend to shift the $[\text{CII}]$ into the cloud where the inset of clumps begins. Hence, the observed stratification profile cannot be reproduced and our density profile becomes useless. Furthermore, line intensities, especially of CO 16-15 and ^{13}CO 10-9 are found to be too low. Increasing the total mass in clumps is not an option as this would strengthen the shift of the $[\text{CII}]$ peak. We find that higher clump densities are better suited to reproduce the line emission and fixed the average clump density to $4 \times 10^6 \text{ cm}^{-3}$. Higher ensemble-averaged densities than $4 \times 10^6 \text{ cm}^{-3}$ could not

be tested, as an ensemble with the single-clump masses chosen here and an averaged density of $4 \times 10^6 \text{ cm}^{-3}$ already contains clumps with densities of about 10^7 cm^{-3} . Clumps with higher densities would drop out of the KOSMA- τ parameter grid.

Spatial variation of clumps: We find that a homogeneous model (containing the same amount of clump and interclump mass in each voxel, here exemplarily model “Hog. 12”) cannot reproduce the observed chemical stratification. In model “Hog. 12” all transitions except for CO 3-2 and CO 2-1 are found to peak at the same y-offset as the $[\text{CII}]$ emission. Investigation of individual clumps for some transitions (for example HCO^+) shows that the strength of the emission strongly correlates with the incident FUV flux as soon as high-density material is present, making a reproduction of the observed chemical stratification based on a homogeneous model impossible. However, Parmar et al. (1991), Hogerheijde et al. (1995) and Young Owl et al. (2000) proposed already a clumpy picture where dense clumps only start at a depth of 10 – 20” into the cloud. Therefore we have used a profile where clumps are only added to the interclump medium at the fourth voxels into the PDR, i.e. 15” behind the IF. It is utilised in the other models from Table 2 except for the homogeneous model “Hog. 12”. The variation in the clump mass per voxel is indicated in the 4th column. Density profiles for the Orion Bar have been discussed by other authors, see Sect. 5.3. In addition to the homogenous model and the reference model “Hog. 1” (with an inset of dense clumps at 0.03 pc depth) a model “Hog. 11” with the inset of clumps starting at 0.04 pc depth (5th row of voxels) has been tested. We find that in terms of stratification this model yields better results than our reference model. All transitions, except for the low- J CO and ^{13}CO , match the observed y-offsets within 0.02 pc or less. However, the line intensities of the high density tracers, especially of CO 16-15, ^{13}CO 10-9 and HCO^+ , cannot be reproduced as the FUV field at 0.04 pc depth into the PDR is already too weak. One possibility is that the model for the FUV extinction by dust, chosen for our model, provides too much FUV extinction for the Orion Bar PDR. Model “Hog. 11”, combined with less FUV extinction might be capable of providing a better fit than our reference model.

In addition to the “Hogerheijde” models we tested a cylindrical geometry as described in the last line of Table 2. The integrated line intensities which have been derived for this model are inconspicuous, i.e., in the range of the intensities that have been derived for the different “Hogerheijde” models. However, in terms of stratification the cylinder turns out to be problematic: the low- J CO and ^{13}CO transitions are peaking very deep into the cloud, as observed for most of the “Hogerheijde” models. However, most of the other transitions are not stratified or even peak in front of $[\text{CII}]$. Therefore, for the given parameter set, we have ruled out the cylinder geometry. A cylinder with less curvature might provide better results.

To achieve a “perfect fit” a model with a more complex density structure might be necessary. A model similar to model “Hog. 11” (clump inset at 0.04 pc depth) but with less FUV extinction close to the IF (enabling the excitation of the high-density tracers inside the PDR) and more FUV extinction at greater depth (to decrease the shift of the low- J CO isotopes) could improve our best model. However, such a complex density profile is beyond the scope of this work.

5.3. Discussion

The most significant conclusions can be drawn from our unsuccessful attempts to simultaneously fit the line intensities and the peak positions measuring the geometrical stratification of the Orion Bar PDR.

We find that a geometry of the Orion Bar region similar to the geometry derived in Hogerheijde et al. (1995) and Jansen et al. (1995) is best suited to reproduce stratification and line intensities of the Orion Bar PDR. We fine-tuned the following parameters: for the depth of the cavity 0.3 pc provides good results. This value lies in the range found in literature (Hogerheijde et al. 1995; Pellegrini et al. 2009; Arab et al. 2012). The illuminating source needs to be close to the outer edge of the cavity, avoiding the presence of cold foreground material for some transitions. For the inclination angle of the Bar we find that 0 or 3 deg provide the best fit, which is small, but still in agreement with literature (Melnick et al. 2012). For the FUV flux at the IF we find that the value given by Jansen et al. (1995), $4.4 \times 10^4 \chi_0$, provides good results.

Our finding of the need for an inhomogeneous model is in agreement with previous models and observations. van der Werf et al. (1996) observed a density increase at $\sim 20''$ from the IF into the cloud (represented by an elongated clump) with a thickness of about $10''$. Parmar et al. (1991) proposed already a clumpy picture of the PDR with an increasing size and number of clumps from the IF into the molecular cloud. This was later adopted by Hogerheijde et al. (1995) and Jansen et al. (1995). A detailed investigation was performed by Young Owl et al. (2000). They found that the Orion Bar is best modelled when incorporating a ridge of dense clumps into a thinner interclump medium at a depth of $20''$. This is in perfect agreement with our model fit of the clumpy structure. We found that the dense clump have to be added to the interclump medium at a depth of 4 voxels, i.e. $15''$, to reproduce the observed chemical stratification.

We find that the observed intensities of the high- J CO lines as well as the HCO^+ lines, especially 6-5, can only be reproduced if most of the mass is contained in the clumps. Increasing the amount of interclump material (while keeping its density constant) would overestimate C II and low- J CO lines and produce too much FUV extinction to excite species peaking at some depth into the cloud. This finding is in contradiction to literature. Hogerheijde et al. (1995) find that the Bar is best described if $\sim 10\%$ of the molecular material is contained in clumps while the other $\sim 90\%$ of the material are contained in a thinner, homogeneous interclump medium. van der Wiel et al. (2009) state that the clumps provide half of the total column density for those molecules that exist in both phases, which probably indicates even more thin interclump medium without molecules.

Our total mass per voxel is about a factor 2.5 higher than the value used in Hogerheijde et al. (1995). The interclump mass per voxel based on Hogerheijde et al. (1995) causes too much FUV extinction and therefore prevents the excitation of the high density traces deep inside the PDR. In addition, after reduction of the interclump mass per voxel allowing for sufficient FUV illumination at the position of the clump ridge, the mass contained in clumps based on Hogerheijde et al. (1995) is found to be too low to provide the observed emission. However, our best fit shows that the depth of the cavity is about 0.03 pc (compared to 0.06 pc in Hogerheijde et al. 1995) so that the total column density remains nearly unchanged.

For the interclump medium densities in the range $n_{\text{H}_2} \approx 3^{+2.0}_{-2.2} 10^4 \text{ cm}^{-3}$ (Hogerheijde et al. 1995), $5 \times 10^4 \text{ cm}^{-3}$ (Young Owl et al. 2000) or $2 \times 10^5 \text{ cm}^{-3}$ (Simon et al. 1997) have been

proposed. We find that a total hydrogen density in the order of $4 \times 10^4 \text{ cm}^{-3}$ gives good results in terms of low- J CO intensities and FUV extinction, which is in coincidence with the range of values stated above. For the clumps we used a density of $4 \times 10^6 \text{ cm}^{-3}$ which is very close to values found in literature, i.e. $n_{\text{H}_2} \approx 1^{+3.0}_{-0.7} 10^6 \text{ cm}^{-3}$ (Hogerheijde et al. 1995), $3 \times 10^6 \text{ cm}^{-3}$ (Young Owl et al. 2000) or between 3×10^6 and $1.2 \times 10^7 \text{ cm}^{-3}$ (assuming that the clumps are virialised, see Lis & Schilke see 2003). In Sect. 3.2 we have discussed that averaging over the Bar in a range of about $30''$ provides a good average over clump and interclump medium. Lis & Schilke (2003) observe the size of dense condensations in the Orion Bar and find sizes between $3.81''$ and $7.96''$ and Young Owl et al. (2000) discuss clumps of $9''$ size, supporting our approach.

In addition we tested a cylindrical geometry as discussed in Arab et al. (2012) or Walmsley et al. (2000). This geometry was found to provide peak line intensities in the range of the “Hogerheijde” models, however, it could not reproduce the observed stratification, the y-offset of most species was actually found to be shifted into the wrong direction.

6. Summary

The observation of high-density, high temperature tracers combined with a layering structure of the Orion Bar spanning over more than $15''$ rules out any description of the PDR in terms of a simple plane-parallel model. PDRs, like molecular clouds, are clumpy and filamentary.

We propose a numerical model that is based on the representation of any PDR by an ensemble of clumps (possibly immersed in a thin interclump medium). Our new PDR model builds on the KOSMA- τ PDR code. It enables us to simulate arbitrary geometries of star forming regions in 3D. The region is modelled using cubic voxels where each voxel is filled with an ensemble of clumps mimicking the fractal ISM. The ensemble properties can vary between different voxels. Using a probabilistic algorithm for the calculation of ensemble-averaged emissivities and opacities allows us to model the radiative transfer on a normal PC. The algorithm is used both to derive the ensemble-averaged FUV extinction for each voxel and to compute the radiative transfer for the emission from the PDR, i.e. the observable line intensities.

As a first test of the new model we performed simulations of the Orion Bar PDR. The simulations tried to simultaneously reproduce the spatial offset of the emission peak seen in the various lines and the integrated intensity for different transitions of CO isotopes, HCO^+ , and $[\text{CII}]$.

Different geometries and parameter combinations have been tried out to simulate the Orion Bar. We find that

- a straight or concave geometry is needed to reproduce the observed stratification. This is in line with the idea of a dense wall of a cavity around the illuminating cluster. A convex filament can be ruled out.
- the main illuminating star $\Theta^1 \text{ Ori D}$ must be located close to the edge of the cavity wall facing the observer to avoid foreground absorption in the mid- to high- J lines. Our fit of depth of the cavity of 0.3 pc agrees with the estimate from van der Werf et al. (2013).
- the estimate for the FUV flux of $4.4 \cdot 10^4 \chi_0$ by Hogerheijde et al. (1995) matches the flux that allowed us to fit the line intensities
- the density of the clumps and the interclump medium are the most critical parameters for the simultaneous fit of the

line intensities and the stratification structure of the Orion Bar. The interclump medium governs the FUV extinction and hence the spatial layering while the clumps produce most of the emission from the molecular tracers. Our fit requires relatively high densities for both components of $4 \cdot 10^4$ and $4 \cdot 10^6 \text{ cm}^{-3}$, respectively.

- to reproduce the line intensities, a large ratio of clump to interclump material is needed. This contradicts the earlier estimates by Hogerheijde et al. (1995).
- in agreement with suggestions from the literature (Parmar et al. 1991; Hogerheijde et al. 1995; Young Owl et al. 2000), a line fit is only possible if we invoke a process that removes dense clumps close to the PDR surface. The detailed stratification profile cannot be reproduced by models with a constant ratio of clump to interclump gas.

In this paper we only compared maps of line intensities with the observations, but the 3D PDR code also allows to simulate all details of the line profiles. A systematic comparison of the profiles to the observations will be discussed in a subsequent paper.

Acknowledgements. We thank D. Lis for providing the CSO data and helpful comments. S. Andree-Labsch thanks the Deutsche Telekom Stiftung and the Bonn-Cologne Graduate School of Physics and Astronomy for support by means of stipends. Modelling of irradiated molecular clouds is carried out within the Collaborative Research Center 956, sub-project C1, funded by the Deutsche Forschungsgemeinschaft (DFG).

References

- Arab, H., Abergel, A., Habart, E., et al. 2012, *A&A*, 541, A19
- Bergin, E. A., Phillips, T. G., Comito, C., et al. 2010, *A&A*, 521, L20
- Bernard-Salas, J., Habart, E., Arab, H., et al. 2012, *A&A*, 538, A37
- Cubick, M. 2005, Diploma thesis, 1. Physikalisches Institut, University of Cologne
- Cubick, M., Stutzki, J., Ossenkopf, V., Kramer, C., & Röllig, M. 2008, *A&A*, 488, 623
- de Graauw, T., Helmich, F. P., Phillips, T. G., et al. 2010, *A&A*, 518, L6
- Draine, B. T. 1978, *ApJS*, 36, 595
- Draine, B. T. 2011, *Physics of the interstellar and intergalactic medium* (Princeton University Press), 326
- Fong, D., Meixner, M., Castro-Carrizo, A., et al. 2001, *A&A*, 367, 652
- Habing, H. J. 1968, *Bull. Astron. Inst. Netherlands*, 19, 421
- Heithausen, A., Bensch, F., Stutzki, J., Falgarone, E., & Panis, J. F. 1998, *A&A*, 331, L65
- Hogerheijde, M. R., Jansen, D. J., & van Dishoeck, E. F. 1995, *A&A*, 294, 792
- Hollenbach, D. J. & Tielens, A. G. G. M. 1999, *Reviews of Modern Physics*, 71, 173
- Howe, J. E., Jaffe, D. T., Genzel, R., & Stacey, G. J. 1991, *ApJ*, 373, 158
- Jansen, D. J., Spaans, M., Hogerheijde, M. R., & van Dishoeck, E. F. 1995, *A&A*, 303, 541
- Lis, D. C. & Schilke, P. 2003, *ApJ*, 597, L145
- Marconi, A., Testi, L., Natta, A., & Walmsley, C. M. 1998, *A&A*, 330, 696
- Martins, F., Schaerer, D., & Hillier, D. J. 2005, *A&A*, 436, 1049
- McCaughrean, M. J. 2002, in *The Origin of Stars and Planets: The VLT View*, ed. J. F. Alves & M. J. McCaughrean, 1
- Melnick, G. J., Tolls, V., Goldsmith, P. F., et al. 2012, *ApJ*, 752, 26
- Menten, K. M., Reid, M. J., Forbrich, J., & Brunthaler, A. 2007, *A&A*, 474, 515
- Müller, H. S. P., Schlöder, F., Stutzki, J., & Winnewisser, G. 2005, *Journal of Molecular Structure*, 742, 215
- Müller, H. S. P., Thorwirth, S., Roth, D. A., & Winnewisser, G. 2001, *A&A*, 370, L49
- Ossenkopf, V., Röllig, M., Cubick, M., & Stutzki, J. 2007, in *Molecules in Space and Laboratory*
- Ossenkopf, V., Röllig, M., Neufeld, D. A., et al. 2013, *A&A*, 550, A57
- Ossenkopf, V., Trojan, C., & Stutzki, J. 2001, *A&A*, 378, 608
- Parmar, P. S., Lacy, J. H., & Achtermann, J. M. 1991, *ApJ*, 372, L25
- Pellegrini, E. W., Baldwin, J. A., Ferland, G. J., Shaw, G., & Heathcote, S. 2009, *ApJ*, 693, 285
- Pilbratt, G. L., Riedinger, J. R., Passvogel, T., et al. 2010, *A&A*, 518, L1
- Roelfsema, P. R., Helmich, F. P., Teyssier, D., et al. 2012, *A&A*, 537, A17
- Röllig, M., Abel, N. P., Bell, T., et al. 2007, *A&A*, 467, 187
- Röllig, M., Ossenkopf, V., Jeyakumar, S., Stutzki, J., & Sternberg, A. 2006, *A&A*, 451, 917
- Röllig, M., Szczerba, R., Ossenkopf, V., & Glück, C. 2013, *A&A*, 549, A85
- Simon, R., Stutzki, J., Sternberg, A., & Winnewisser, G. 1997, *A&A*, 327, L9
- Stahl, O., Wade, G., Petit, V., Stober, B., & Schanne, L. 2008, *A&A*, 487, 323
- Sternberg, A. 2004, in *Astronomical Society of the Pacific Conference Series*, Vol. 323, *Star Formation in the Interstellar Medium: In Honor of David Hollenbach*, ed. D. Johnstone, F. C. Adams, D. N. C. Lin, D. A. Neufeld, & E. C. Ostriker, 149
- Stutzki, J., Bensch, F., Heithausen, A., Ossenkopf, V., & Zielinsky, M. 1998, *A&A*, 336, 697
- Stutzki, J. & Guesten, R. 1990, *ApJ*, 356, 513
- Stutzki, J., Stacey, G. J., Genzel, R., et al. 1988, *ApJ*, 332, 379
- Tielens, A. G. G. M. & Hollenbach, D. 1985, *ApJ*, 291, 722
- Tielens, A. G. G. M., Meixner, M. M., van der Werf, P. P., et al. 1993, *Science*, 262, 86
- van der Tak, F. F. S., Nagy, Z., Ossenkopf, V., et al. 2013, *A&A*, 560, A95
- van der Werf, P. P., Goss, W. M., & O'Dell, C. R. 2013, *ApJ*, 762, 101
- van der Werf, P. P., Stutzki, J., Sternberg, A., & Krabbe, A. 1996, *A&A*, 313, 633
- van der Wiel, M. H. D., van der Tak, F. F. S., Ossenkopf, V., et al. 2009, *A&A*, 498, 161
- Walmsley, C. M., Natta, A., Oliva, E., & Testi, L. 2000, *A&A*, 364, 301
- Weingartner, J. C. & Draine, B. T. 2001, *ApJ*, 548, 296
- Wen, Z. & O'dell, C. R. 1995, *ApJ*, 438, 784
- Young Owl, R. C., Meixner, M. M., Wolfire, M., Tielens, A. G. G. M., & Tauber, J. 2000, *ApJ*, 540, 886

Appendix A: Testing the probabilistic approach

In Sect. 2.3.3 ensemble-averaged opacities (and emissivities) have been derived based on binomial distributions. This formalism was verified using a direct approach to calculate ensemble-averaged entities (presented here exemplarily for the average opacity of the [CII] line). As the direct approach requires a relatively large amount of computing time it is not used in the simulations of the 3D geometry, where ensemble-averaged entities need to be calculated for about 10^5 different ensembles. However, we used it to calculate the ensemble-averaged opacity of selected ensembles with known parameters to be compared to the results of the “binomial” approach.

This serves three purposes:

- to verify that the calculation of the ensemble-averaged opacity through the probabilistic approach matches the average opacity of real random realisations (random positions for each clump) of the ensemble
- to verify that averaging over the clump projected area (compare Eq. 5) can be used (the method presented here accounts for the full “opacity profile” $\tau_{cl}(p)$ with p being the *impact parameter*, or radial distance from the centre point of the clump)
- for statistical reasons, i.e. to understand how much the ensemble-averaged opacity of the same ensemble can vary depending on the random positions of the individual clumps.

As discussed in Sect. 2.3.1 we consider randomly distributed clumps of masses M_j with a fixed area filling factor $N'_j/(\Delta s')^2$. The projected surfaces of the clumps may overlap. A section of the projected surface of such an ensemble is shown in Fig. A.1 for an ensemble of clumps with masses $\{M_j\}_{j=1...n_M} = \{10^0, 10^{-1}, 10^{-2}, 10^{-3} M_\odot\}$ and a total mass of $0.00346 M_\odot$ per $(0.01 \text{ pc})^2$ projected surface area (which translates into $N'_j/(\Delta s')^2$ using Eq. 19). The ensemble averaged density in Fig. A.1 has been fixed to be $4 \times 10^6 \text{ cm}^{-3}$, densities of individual clumps have been calculated using Eq. 18. The incident FUV flux has been chosen to be $10^4 \chi_0$.

The colour scale of Fig. A.1 shows the line extinction $e^{-\tau}$ for the example of the line averaged [CII] optical depth summed up along lines of sight perpendicular to the printed surface. The

“opacity profile” $\tau_{cl}(p)$ of the individual clumps is clearly visible: as expected the [CII] line opacity is highest in the outer layers of each clump.

The “opacity map”, Fig. A.1, has been derived on a spatial grid with a grid-spacing $d_{grid} \ll \Delta s'$ (Fig. A.1 contains $n_{grid} = 1184 \times 1184$ grid points). The ensemble-averaged opacity $\overline{e^{-\tau}}$ for this representation of the ensemble is calculated using

$$\overline{e^{-\tau}} = \frac{1}{n_{grid}} \sum_{k=0}^{n_{grid}} e^{-\tau_k}. \quad (A.1)$$

The resulting $\overline{e^{-\tau}}$ can be compared to the result of the “binomial” approach (Eq. 27).

Exemplarily, ensemble-averaged optical depths, $\tau = -\ln(\overline{e^{-\tau}})$, have been derived for 20 different realisations of the ensemble with the parameters described above. In ten cases “opacity maps” of the size shown Fig. A.1 have been simulated, and for the other ten realisations the “opacity maps” are larger ($n_{grid} = 1741 \times 1741$). The resulting τ ’s are indicated by the circles and squares in Fig. A.2 and show some scatter for the different realisations. As expected, the scatter is larger for the smaller maps. The black line in Fig. A.2 gives the opacity averaged over the 20 values and the red, dashed line shows the result for the same ensemble calculated from the “binomial approach”. In the calculation of the averaged value the maps got different weights, depending on their respective number of pixels.

Similar comparisons have been performed for different profiles, $\tau_{cl}(p)$, for different chemical species and transitions, clump parameters, and beam filling factors.

The reliability of the approach presented here depends on the size of the calculated “opacity maps” or equally on the number of representations of the ensemble to be averaged over. As expected the agreement between the two methods increases when more representations of the ensemble are used. The deviation between the averaged optical depths calculated with the two different approaches in Fig. A.2 (the two lines) is about 6%. For other ensembles with the densities of the individual clumps lying on the parameter grid, i.e. where we do not need to interpolate between the profiles, $\tau_{cl}(p)$, the agreement has always been better than 3%.

Appendix B: Radiative transport: numerical solution

The radiative transfer equation with linearised variation of the emission and absorption coefficients ϵ and κ , Eq. 34. Integration over the spatial distance s yields

$$I = \frac{1}{e^{k_0 \cdot \Delta s + \frac{1}{2} k_1 \cdot (\Delta s)^2}} \left\{ \frac{e_1}{k_1} \left[\left(1 - e^{-k_0 \Delta s - \frac{1}{2} k_1 (\Delta s)^2} \right) + \sqrt{\frac{\pi}{2}} \frac{k_0}{\sqrt{k_1}} e^{k_0 \cdot \Delta s + \frac{1}{2} k_1 \cdot (\Delta s)^2} \frac{b_0^2}{2k_1} \right] \right. \\ \left. - \sqrt{\frac{\pi}{2}} \frac{e_1}{\sqrt{k_1}} e^{k_0 \cdot \Delta s + \frac{1}{2} k_1 \cdot (\Delta s)^2} \frac{k_0^2}{2k_1} d \right\} \\ \cdot \left(\operatorname{erfi} \left(\frac{k_0}{\sqrt{2k_1}} \right) - \operatorname{erfi} \left(\frac{k_0 + k_1 \Delta s}{\sqrt{2k_1}} \right) \right) - \sqrt{\frac{\pi}{2}} \frac{e_1}{\sqrt{k_1}} e^{k_0 \cdot \Delta s + \frac{1}{2} k_1 \cdot (\Delta s)^2} \frac{k_0^2}{2k_1} d \\ \cdot \left(\operatorname{erfi} \left(\frac{k_0}{\sqrt{2k_1}} \right) - \operatorname{erfi} \left(\frac{k_0 + k_1 \Delta s}{\sqrt{2k_1}} \right) \right) + I_{bg} \Bigg\} \\ =: \frac{1}{e^{k_0 \cdot \Delta s + \frac{1}{2} k_1 \cdot (\Delta s)^2}} \left\{ \tilde{I} + I_{bg} \right\} \quad (B.1)$$

where $\operatorname{erfi}(\dots)$ denotes the imaginary Error Function (integration by Wolfram Mathematica⁹). Subsequent substitution of

$$a := \frac{k_0}{\sqrt{2k_1}} \\ b := \sqrt{\frac{k_1}{2}} \cdot \Delta s \\ c := \sqrt{\frac{\pi}{2}} \frac{e_1}{\sqrt{k_1}} \\ d := \frac{e_1}{k_1} \quad (B.2)$$

yields an expression of the form

$$\tilde{I} = d \cdot f_1(a, b) - c \cdot f_2(a, b). \quad (B.3)$$

⁹ <http://www.wolfram.com/mathematica/>

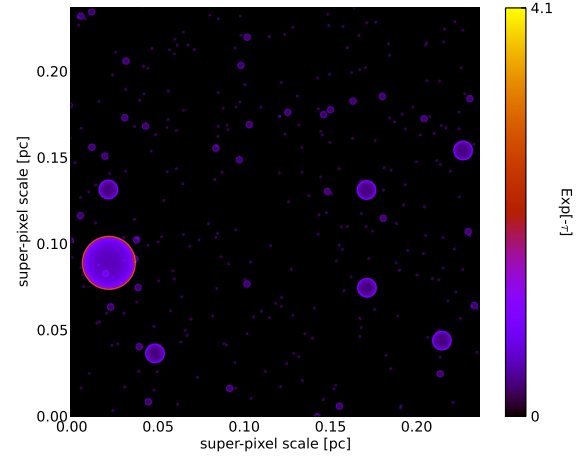


Fig. A.1. One representation of the ensemble described in the text, consisting of randomly distributed clump. The colour scale gives the line extinction $e^{-\tau}$, here exemplarily for the 1.9 THz [CII] transition, where the line absorption is highest in the outer layer of each clump.

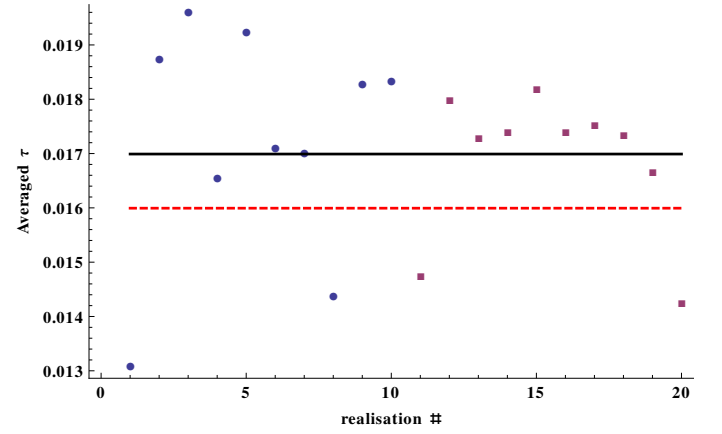


Fig. A.2. Ensemble-averaged optical depths, τ . the circles show the ensemble-averaged τ ’s of ten different “opacity maps” as presented in Fig. A.1 and the squares give the values for ten different “opacity maps” with $n_{grid} = 1741 \times 1741$. The black line gives the mean value of the 20 maps, weighted by the respective number of grid points. The red, dashed line gives the value derived by the “binomial approach” for the same ensemble.

The functions $f_1(a, b)$ and $f_2(a, b)$ are defined by

$$f_1(a, b) = \left(1 - e^{-2ab-b^2}\right) + \sqrt{\pi}ae^{-2ab-b^2-a^2} \cdot \left(\operatorname{erfi}(a) - \operatorname{erfi}(a+b)\right) \quad (\text{B.4})$$

$$f_2(a, b) = e^{-2ab-b^2-a^2} \cdot \left(\operatorname{erfi}(a) - \operatorname{erfi}(a+b)\right).$$

and have been tabulated to enable a fast computation.

Appendix C: FUV flux at the ionisation front

Jansen et al. (1995) state that the radiation field incident on the Orion Bar corresponds to an enhancement over the average interstellar radiation field, χ_0 , of a factor $\approx 4.4 \cdot 10^4$. Other authors give similar values, Marconi et al. (1998) estimate a flux of $1 - 3 \cdot 10^4$ times the average interstellar field. Arab et al. (2012); Young Owl et al. (2000); Walmsley et al. (2000) used $1 - 4 \cdot G_0$ at the IF with G_0 being the Habing field (Habing 1968)¹⁰.

Here, we have re-estimated the FUV flux at the IF, originating from Θ^1 Ori C, based on synthesised stellar spectra provided by Martins et al. (2005)¹¹. Different spectra from their sample have been investigated, for stars having effective temperatures between 35000 and 39540 K which covers the spectral classes from O7V to O6V. Different authors (Stahl et al. 2008; Pellegrini et al. 2009; Arab et al. 2012) obtained varying results for the spectral class of Θ^1 Ori C, but it clearly falls in the range between O6 through O7.

The selected spectra have been integrated in the FUV range, 2066 to 911 Å (6 to 13.6 eV), and the resulting flux at the position of the Orion Bar has been computed. For this calculation, the distance between Θ^1 Ori C and the Orion Bar has been assumed to be 0.223 pc, i.e. equal to the projected distance (neglecting a possible offset in radial direction which is not precisely known, compare Sect. 3.1). The calculated fluxes fall between 17 and 373 erg s⁻¹ cm⁻² ($0.63 \cdot 10^4 \chi_0 - 13.8 \cdot 10^4 \chi_0$), covering the range of values discussed above.

In our simulations we started with a value representative for an O6.5 star ($T_{\text{eff}}=36826$ K, Martins et al. 2005) providing a flux of 38 erg s⁻¹ cm⁻² or $1.4 \cdot 10^4 \chi_0$ at the IF. However, with this value it was impossible to reproduce the observed intensities of the high- J CO and HCO⁺ lines (see Sect. 5.1). In contrast, the value of $4.4 \cdot 10^4 \chi_0$ from Jansen et al. (1995) allowed for a decent fit. This is best reproduced by the star from the sample with $T_{\text{eff}}=37760$ K, which indicates the spectral class O6.5V (Martins et al. 2005).

¹⁰ The difference between the Draine field χ_0 and the Habing field G_0 is $\chi_0/G_0 \approx 1.7$

¹¹ available online: <http://www.mpe.mpg.de/~martins/SED.html>